

**Infrared-terahertz double resonance spectroscopy
of CH₃F and CH₃Cl at atmospheric pressure**

Dane J. Phillips,^{*} Elizabeth A. Tanner,[†] Frank C. De Lucia,[‡] and Henry O. Everitt[§]

^{*} *Kratos – Digital Fusion, 4904 Research Drive, Huntsville, AL 35805, USA*

[†] *IERUS Technologies, 2904 Westcorp Blvd. Ste 210, Huntsville, AL 35805*

[‡] *Department of Physics, 191 Woodruff Ave., The Ohio State University, Columbus, OH 43210*

[§] *Charles M. Bowden Laboratory, Army Aviation and Missile RD&E Center, Redstone Arsenal, AL 35898*

Abstract

A new method for highly selective remote sensing of atmospheric trace polar molecular gases is described. Based on infrared/terahertz double resonance spectroscopic techniques, the molecule-specific coincidence between the lines of a CO₂ laser and rotational-vibrational molecular absorption transitions provide two dimensions of recognition specificity: infrared coincidence frequency and the corresponding terahertz frequency whose absorption strength is modulated by the laser. Atmospheric pressure broadening expands the molecular recognition “specificity matrix” by simultaneously relaxing the infrared coincidence requirement and strengthening the corresponding terahertz signature. Representative double resonance spectra are calculated for prototypical molecules CH₃F and CH₃Cl and their principal isotopomers, from which a heuristic model is developed to estimate the specificity matrix and double resonance signature strength for any polar molecule.

Receipt date: ???

PACS indexing codes: 33.20.-t, 33.40.+f

I. INTRODUCTION

Double resonance (DR) techniques are widely used in all phases of optical spectroscopy, from ultrafast pump/probe and excitation correlation measurements in the ultraviolet/visible/infrared spectral regions to investigations of molecular collisional physics in the microwave/microwave and infrared/millimeter wave regions [1 - 7]. Although wavelength-degenerate DR techniques provide some insight into the relaxation dynamics from a photoexcited state, wavelength-nondegenerate DR techniques - which rely on the ability to tune the frequencies of the pump and probe beams independently - provide greater insight into energy transfer pathways and rates [8 - 11]. Sometimes, the limited frequency tunability of pump or probe sources limits the effectiveness of DR techniques. For example, optically pumped far infrared lasers - which use a line-tunable CO₂ infrared (IR) laser to excite a terahertz (THz) rotational population inversion in a low pressure gas - are constrained by the rare coincidence (< 100 MHz) between any CO₂ laser line and any molecular rotational-vibrational IR transition [12 - 14]. This rare coincidence forces optically pumped far-IR (OPFIR) lasers to operate on only a few THz frequencies per molecule, but as the gas pressure and corresponding IR and THz linewidths increase, greater tunability and spectral coverage is possible [15 - 20].

Recently we have proposed that the IR/THz DR technique may be adapted for remote sensing of trace gases in the atmosphere if IR pulses of sufficiently short duration (~ 100 ps) can be generated [21]. In particular, it was shown that a 100 m thick cloud of CH₃F with a uniform concentration of 1 ppm (~1 mTorr partial pressure) could be detected using a THz transceiver tuned to the frequency of the IR pump-induced THz DR signature. Detection occurs through the co-propagation of IR pump and THz probe beams through the trace gas cloud to a retro-

reflecting surface up to 1 km away. If absorbed by the trace gas, the pulsed IR pump beam briefly alters the absorption strength of the returned continuous wave THz probe beam, and this repeating modulation may be detected at the pulse repetition frequency of the laser. The actual sensitivity of this technique depends in a complex manner upon the IR and THz absorption coefficients of the molecule and the atmospheric water vapor content. Recognition specificity is achieved through the molecule-unique combination of IR pump coincidence frequency and the frequency of the pump-induced change in the THz signature. For a given molecule, only a few of its hundreds of IR ro-vibrational transitions are coincident with any CO₂ laser line, and each rare coincidence produces a unique pump-induced absorption change in a few of the hundreds of THz rotational transition frequencies. These two dimensions of recognition (IR pump and THz DR frequencies) comprise a “specificity matrix” whose sparseness can be used to identify an atmospheric trace gas remotely with enough spectral discrimination that even isotopomers may be distinguished.

One of the findings of that study [21] is that the coincidence requirement between CO₂ laser and IR molecular transition is relaxed when the trace gas primarily collides with atmospheric pressure gases (see Figure 1). Specifically, Figure 2 indicates that the ro-vibrational IR linewidth of CH₃F evolves from a Doppler-broadened $\Delta\nu_D = 33$ MHz (half-width at half-maximum, or HWHM) for low pressure operation (typical of OPFIR lasers) to a pressure broadened $\Delta\nu_P \approx 3$ MHz/Torr = 2.3 GHz HWHM when the same 1 mTorr of gas is in an atmosphere of N₂ and O₂ [22]. Moreover, the IR linewidth function changes from Gaussian to Lorentzian, meaning that the spectral overlap falls off less abruptly with frequency at atmospheric pressure. This broadening relaxes the pump coincidence requirement from those ro-vibrational lines within 66 MHz of a CO₂ laser line (spaced 24 to 69 GHz apart, see Figure 1a) to

those within 4.6 GHz [23]. The benefit is that favorable IR/THz pump/probe combinations, including transitions that are not accessible at low pressure, may be selected for atmospheric remote sensing.

In order to explore the molecule-unique signatures that constitute the recognition specificity matrix, we calculate the double resonance signatures of all IR/THz pump/probe coincidences at atmospheric pressure for $^{12}\text{CH}_3\text{F}$ and $\text{CH}_3^{35}\text{Cl}$ and their principal isotopomers $^{13}\text{CH}_3\text{F}$ and $\text{CH}_3^{37}\text{Cl}$ that are 1% and 24% abundant, respectively. These molecules were chosen as prototypical because their excited vibrational levels are well isolated but different in nature: a CO_2 laser that is line tunable over 9-11 μm wavelength region ($900\text{-}1100\text{ cm}^{-1}$) excites the V_3 stretching mode of CH_3F and the V_6 bending mode of CH_3Cl . We will show that the DR signatures are dramatically different for these two types of vibrational states in ways that are unique to the molecule, providing additional recognition specificity. Because many new coincidences occur at atmospheric pressure, we show how to estimate the strength of the DR signals so that the IR/THz combinations most useful for remote sensing may be identified.

II. DOUBLE RESONANCE SPECTROSCOPY

A. Pump Coincidences

The energy levels of the ground and excited vibrational states of CH_3F and CH_3Cl were calculated using the rotational constants listed in Tables I and II. For CH_3F , the standard P-type ($\Delta J = -1$), Q-type ($\Delta J = 0$), and R-type ($\Delta J = +1$) transitions from ground state to the V_3 vibrational level produce a classic stretching mode spectrum (Figure 1b) whose absorption strengths are determined by a combination of the ground state's fraction of the temperature-

dependent partition function, quantum mechanical transition matrix element (Table III), and dipole derivative for the vibrational transition. The notation for a ro-vibrational transition is $X_K(J)$, where J,K designate the rotational state of origin in the ground vibrational level and X = P, Q, or R depending on the type of ro-vibrational transition excited.

By comparison, the spectrum of the V_6 bending mode is characterized by l -doubling that couples the bending motion $l = \pm 1$ with the rotation designated by the K quantum number. The notation is modified to $^Y X_K(J)$ to account for whether the ro-vibrational transition excited in V_6 satisfies $l = +1$ ($Y = R$) or -1 ($Y = P$). The corresponding spectrum (Figure 1c) is remarkably different than for the bending mode in CH_3F because l -doubling breaks the $\pm K$ degeneracy, dramatically affecting the energy level structure and transition matrix elements (Table III). An examination of a partial low pressure rotational spectrum of these two excited states (Figures 1d & 1e) shows the effects of l -doubling and hyperfine splitting in CH_3Cl . (Hyperfine splittings in CH_3Cl that are resolved at low pressure may be ignored at the atmospheric pressures of interest here.)

Using these calculated energy levels, the allowed IR ro-vibrational transition frequencies were calculated and compared with the known frequencies produced by line-tunable CO_2 lasers [23]. To find nearly overlapping coincidences, assume for the moment that the IR pump is a continuous wave CO_2 laser so the coincidence occurs within the linewidth of the molecular ro-vibrational transition. For a pure, 1 mTorr gas of CH_3F or CH_3Cl at 300K, the salient IR ro-vibrational transition is Doppler broadened with a Gaussian HWHM linewidth $\Delta\nu_D$ of 33.4 MHz and 27.4 MHz, respectively [24]. All ro-vibrational IR frequencies are then calculated, and the “offset” frequencies $\nu_{IR} - \nu_{pump}$ of those nearly coincident with specific CO_2 laser lines are compared with the values known from extensive research in OPFIR lasers [25, 26]. The results,

shown in Table IV, indicate the offset frequencies are in good agreement when the vibrational energies in Table I are used. As a notation to simplify the discussion, the rotational states connected by the pump are labeled (J_p, K_p, V_0) and (J_p', K_p', V_i) . The principal rotational transitions exhibiting THz DR signatures, involving the two pairs of adjacent rotational states $(J_p \pm 1, K_p, V_0)$ and $(J_p' \pm 1, K_p', V_i)$, are labeled R_0^- and R_0^+ , R_i^- and R_i^+ , respectively (see Figure 3). The frequencies of these four rotational transitions are presented in Table IV.

Next, the ro-vibrational transitions of CH_3F or CH_3Cl with 1 mTorr of partial pressure are broadened by an atmosphere of N_2 and O_2 (i.e. concentration $\theta \sim 1$ ppm of analyte), and the coincidence calculation is repeated. Using a pressure broadening parameter of 3 MHz/Torr FWHM - typical for hard shell collisions with non-polar molecules [22] - the estimated linewidth of $\Delta\nu_p = 2.3$ GHz HWHM far exceeds the Doppler-broadened linewidth. Using a Lorentzian lineshape function with this linewidth parameter, the overlap expands and many new coincidences are found.

Table V lists only those coincidences in $^{12}\text{CH}_3\text{F}$ and $^{13}\text{CH}_3\text{F}$ whose overlap with the CO_2 laser is within one atmospheric pressure-broadened Lorentzian linewidth of the ro-vibrational center frequency. Of the new ro-vibrational coincidences that arise, many involve CO_2 lines that experience no low pressure coincidences, while the rest represent additional coincidences with CO_2 lines already known to have a low pressure coincidence. In both cases, atmospheric pressure broadening of the ro-vibrational transitions often causes a given laser line to excite many rotational states simultaneously. The four rotational frequencies reported in Table V correspond to the ro-vibrational transition whose $(J_p, K_p, V_0) \rightarrow (J_p', K_p', V_i)$ transition most closely coincides with the strongest modulated terahertz absorption.

B. Differential Absorption

The strength of the pump-induced THz DR signatures may be calculated from the standard equation for molecular absorption [24, 27]

$$\begin{aligned}\alpha &= \frac{8\pi^3}{3hc} \nu (n_L - n_U) |\mu|^2 S(\nu, \nu_0) \\ &= 3.24 \times 10^{-6} \frac{\nu}{\Delta\nu} (f_L - f_U) \theta |\langle U | \mu_t | L \rangle|^2 \text{ cm}^{-1},\end{aligned}\quad (1)$$

where ν is the frequency (GHz) of the transition and $n_i = 2.45 \times 10^{13} f_i \theta \text{ cm}^{-3}$ is the population of the molecular states connected by the probe and pump ($i = L, U$) for a non-degenerate fractional state population f_i and concentration θ ppm at 300K in an ambient atmosphere of 760 Torr. The factor containing μ_t is the dipole matrix element for this transition (Debye), and $S(\nu, \nu_0)$ is the lineshape function that simplifies to $1/\pi\Delta\nu$ (GHz⁻¹) at the peak of a pressure-broadened Lorentzian lineshape [28, 29]. The absorption α_{THz} at ν_{THz} arises from rotational transitions mediated by the permanent dipole moment of the molecule ($\mu_t = \mu$), while the absorption α_{IR} at ν_{IR} arises from ro-vibrational transitions mediated by the appropriate dipole moment derivative along the respective normal coordinate (Q_i) for the corresponding excited vibrational level ($\mu = d\mu/dQ_i$) [28].

Note that the absorption coefficient is proportional to the square of the appropriate dipole moment mediating the transition, multiplied by the rotational transition branching ratio $0 < |\langle U | \mu | L \rangle|^2 < 1$ given in Table III [30]. For IR transitions, the dipole derivative can be a factor of 10 (stretching modes) to 100 (bending modes) times weaker than the dipole moment itself, an effect that will tremendously affect DR spectroscopy. Specifically, $\mu = 1.86 \text{ D}$ and $d\mu/dQ_i =$

0.2756 D for the CH₃F V₃ transition, while $\mu = 1.90$ D and $d\mu/dQ_6 = -0.0388$ D for the CH₃Cl V₆ transition [29 - 31]. Consequently, the IR transition absorption strength is approximately two orders of magnitude stronger in the stretching V₃ mode than in the bending V₆ mode. This difference arises because of the type of motion involved, not because of the differing masses of the two molecules, suggesting a more universal insight: DR signatures will generally be stronger in stretching modes than bending modes. Unfortunately, molecules tend to have more bending modes than stretching modes, which can be challenging if those modes span the region over which a CO₂ laser can be tuned.

The strength of the pump-induced THz DR signature may now be estimated. For an optically thin cloud ($\alpha_{THz}d \ll 1$) diluted in air to concentration θ with IR optical depth $\alpha_{IR}d \ll 1$, the total number of photons absorbed (i.e. the number of molecules photo-excited per pulse) is

$$N_{pumped} = \frac{\varepsilon}{h\nu_{IR}} \alpha_{IR} d, \quad (2)$$

where ε is the pump energy per pulse (J), d is the path length of the laser in the cloud, and α_{IR} can be calculated from (1) with the assumption $n_U \approx 0$. From this, it is easy to show that the fraction of the n_L molecules pumped per laser pulse in a beam of radius r_{IR} (m) is

$$f_{pumped} = \frac{\varepsilon \alpha_{IR}}{(\pi r_{IR}^2)(h\nu_{IR})n_L} = 6.35 \frac{\left| \left\langle U \left| \frac{d\mu}{dQ} \right| L \right\rangle \right|^2}{\Delta\nu_{IR} r_{IR}^2} \varepsilon, \quad (3)$$

where the transition matrix for this ro-vibrational transition is the product of the square of the corresponding dipole derivative (Debye) and the appropriate transition branching ratio Table III.

These calculations assume there is no pump saturation, but for highly intense pump beams saturation effects must be considered.

If the DR signature is observed on a time scale shorter than the collisional relaxation time (~ 100 ps at atmospheric pressure), then the only rotational transitions with photo-induced population changes are R_0^+ , R_0^- , R_i^+ , and R_i^- (Figure 3). The pump-induced change in the absorption coefficients (1) arises from a change in the associated population differences from equilibrium ($n_L - n_U$) to pumped ($n_L \pm \Delta n - n_U$) values, where $\Delta n = N_{pumped}/V_{IR}$ and $V_{IR} = \pi r_{IR}^2 d$ is the volume occupied by the IR beam inside the gas. The measured THz DR spectrum is the pump-induced change in the rotational absorption coefficient

$$\Delta\alpha = \pm \frac{8\pi^2}{3h^2c} \left[\frac{\nu_{THz}}{\Delta\nu_{THz}} \left| \langle U | \mu | L \rangle \right|^2 \right] \left[\frac{\Delta\nu_{IR}}{\Delta\nu_{IR} + (\nu_{IR} - \nu_{pump})^2} \frac{\alpha_{IR}}{\nu_{IR} (\pi r_{IR}^2)} \varepsilon \right], \quad (4)$$

derived from (1) and (2) as a product of terms that depend on the rotational transition (first bracket) and on the ro-vibrational transition (second bracket), where ν_{THz} corresponds to the monitored rotational transition with the indicated transition matrix element. Notice that a Lorentzian lineshape factor has been added to account for the reduced IR absorption caused by the offset (reported in Table V) between the pump and the atmospheric pressure broadened ro-vibrational transition frequencies. (Figure 2 indicates the pressure at which the Lorentzian lineshape must be replaced by a Gaussian.) Because $\Delta\alpha$ grows linearly with IR pump energy (ε) per pulse, the DR absorption strengths are reported as $\Delta\alpha/\varepsilon$ in units of $\text{kJ}^{-1} \text{km}^{-1}$ in Table V.

C. Overlap Enhancement

Since the THz rotational transitions undergo the same pressure broadening as the IR ro-vibrational transitions, the THz DR spectra of nearby pumped rotational transitions may also overlap. This overlap may strengthen or weaken the THz DR signal from the low pressure value (Eq. (4)) in which only one ro-vibrational transition is pumped. The multiplicative factor by which a given transition is strengthened or weakened is significantly less than the number of overlapping transitions because the constituent line strengths may have differing degeneracies and thermal populations, as well as overlaps with the opposite sign of $\Delta\alpha_j$. (For a given laser line, the overlapping transitions in CH₃F are labeled by the subscripts in the ‘‘IR Transition’’ column of Tables IV and V.) The overlap enhancement factor in Table V

$$\Pi(\nu_j) = \frac{\sum_{i=1}^n \Delta\alpha_i \frac{(\Delta\nu_p)^2}{(\nu_i - \nu_j)^2 + (\Delta\nu_p)^2}}{\Delta\alpha_j}, \quad (5)$$

estimates how many times stronger or weaker the DR signal $\Delta\alpha_j$ will be at frequency ν_j because of the overlap from nearby DR features of strength $\Delta\alpha_i$ located at ν_i . Here, the summation is over all n DR signatures associated with all IR transitions excited by a given laser line, where the $\Delta\alpha_i$ and $\Delta\alpha_j$ are calculated in (4). When the THz transitions overlap, the largest $\Delta\alpha_j$ necessarily produces the smallest value of $\Pi(\nu)$ at the transition labeled {R}, so this is the value provided in Table V. The peak of the summed DR signature will be near $\nu_{\{R\}}$, so this is the most appropriate frequency to use for the THz probe.

The product $\Delta\alpha_j \Pi(\nu_j) / \varepsilon$ represents the final estimate of the THz DR strength for a given IR/THz combination in the specificity matrix. This product can be used to ascertain which of the old or new coincidences are most promising for remote sensing for a given isotopomer.

Remember that $\Delta\alpha_j I(\nu_j)$, which may be positive or negative, represents a pump energy-dependent (ε) increase or decrease in the ambient THz absorption strength as $\alpha_{\text{THz}}(\nu_j) \rightarrow \alpha_{\text{THz}}(\nu_j) + \Delta\alpha_j I(\nu_j)$. Although usually observed as a short-lived pump-induced change in absorption strength, THz emission can actually occur when $-\Delta\alpha_j I(\nu_j) > \alpha_{\text{THz}}(\nu_j)$. Because atmospheric collisional redistribution of population is minimal on timescales shorter than 100 ps, $\Delta\alpha_j I(\nu_j)/\varepsilon$ only depends on the absorption strength of the IR ro-vibrational molecular transition, the detuning of the spectral overlap with the nearest CO₂ laser line, and the aggregate strength of the overlapping rotational transitions involving states simultaneously excited by the laser ($I(\nu_j)$). Note that the absorption strength of the IR ro-vibrational transition depends on the type of vibrational mode for a given molecule (dipole derivative for stretching or bending modes), the specific ro-vibrational transition type involved (branching ratios for P, Q, or R), and the rotational partition function (or more precisely, the ground rotational state population n_L of the pumped ro-vibrational transition). Not surprisingly, the optimal ro-vibrational transitions for DR spectroscopy are those with the strongest IR absorption, *i.e.* those nearest the peak of the IR spectrum.

Finally, it has already been pointed out that the pressure-broadened Lorentzian lineshape function falls off less abruptly than the Doppler-broadened Gaussian lineshape function, so overlaps are more readily excited. The decision to include only those overlaps within one linewidth $\Delta\nu_{\text{IR}}$ of the ro-vibrational line center was arbitrary. Recall the calculation assumed the CO₂ laser was operating continuously; however, if the laser is pulsed, the increased spectral bandwidth of the laser pulses should also be considered in the coincidence calculation. For the remote sensing application, pump pulses of duration comparable to the hard shell gas kinetic collision time (~ 100 ps) are required, corresponding to a spectral bandwidth of 10 GHz that is

(not coincidentally) comparable to the pressure-broadened linewidth $\Delta\nu_p$ of the IR ro-vibrational transition. Clearly even more coincidences may be excited when such short pulses are used, but the pump efficiency is reduced by the fraction of pump radiation that falls outside the spectral bandwidth of the IR absorption line.

III. SPECIFIC EXAMPLES

Having outlined the basic principles underlying the excitation of a DR signal, we next explore the variety of DR signal types, their strengths, and how they depend on the type of photo-excited ro-vibrational transition (Figure 3). Again, we will restrict ourselves to photoexcitation on timescales short compared to the fastest collisional relaxation time of the molecule (~ 100 ps), so only rotational transitions R_0^- , R_0^+ , R_i^- , and R_i^+ are involved.

A. Methyl Fluoride

We start with the simpler case, CH_3F , for which the stretching mode ν_3 of both $^{12}\text{CH}_3\text{F}$ and $^{13}\text{CH}_3\text{F}$ isotopomers is photo-excited by a CO_2 laser. Considering first $^{12}\text{CH}_3\text{F}$, the 9P(20) line of a CO_2 laser is known to photo-excite the $\text{Q}_2(12)$ (and perhaps the $\text{Q}_1(12)$) transition at low pressure. The resulting DR signature has components at 612.409 (R_0^-), 663.365 (R_0^+), 604.297 (R_3^-), and 654.582 GHz (R_3^+). The absorption decreases ($\Delta\alpha_j < 0$) in transitions R_0^+ and R_3^- and increases ($\Delta\alpha_j > 0$) in transitions R_0^- and R_3^+ (Figures 3, 4a), illustrating that a characteristic Q-branch THz DR signature consists of four spectral features in the form of conjugate doublets (two R^- and two R^+) separated by $\sim 2B \approx 51$ GHz. Assuming there is no IR pump saturation,

equation (4) indicates the strengths of these four DR features are linearly proportional to the pump pulse intensity, their THz frequency, and the associated branching ratios (Table III). Each doublet consists of the identical rotational transitions in V_0 and V_3 separated in frequency by $\sim 2(B_3 - B_0)(J + 1)$, a separation of 8.1 GHz for $J = 11 \rightarrow 12$ and 8.8 GHz for $J = 12 \rightarrow 13$. Given that $\Delta\nu_p = 2.3$ GHz, these four features are well resolved at atmospheric pressure.

As noted above, the atmospheric pressure broadened width of the ro-vibrational transitions allows a given laser line to photoexcite many neighboring transitions, primarily those transitions with differing K values, further increasing the strength of the DR signature. In $^{12}\text{CH}_3\text{F}$, the 9P(20) laser line now coincides with nine additional atmospheric pressure broadened ro-vibrational transitions ($Q_1(12) - Q_7(12)$, $Q_{13}(13)$, and $P_0(1)$). When a series of transitions with constant J but varying K are pumped (e.g. $Q_1(12) - Q_7(12)$), it is listed as a single entry in Table V with $\{R\} = \{K\}$ for the transition with smallest $\Pi(\nu_j)$. Figure 2 shows how the multiplier $\Pi(\nu_K)$ for each of the $Q_K(12)$ transitions ($K = 1-7$) grows with increasing pressure, and Figure 4a and 5a show how their aggregate DR signature is the sum of all the constituent, overlapping Q-branch signatures for a portion of the THz region. Notice that $\Pi(\nu_j) = 1$ for $Q_2(12)$ until the pressure broadening exceeds the Doppler broadening of the IR transition, after which there is a rapid, often non-monotonic growth in $\Pi(\nu_j)$ for all transitions as pressure increases. Notice $\Pi(\nu_j)$ for $\{K\} = 6$ only reaches 3.04 at atmospheric pressure, not the theoretical maximum of 6.15 if all seven K levels were equally populated and equally pumped. This reduction occurs because of two effects: the unfavorable branching ratios for low- K Q-branch transitions and the greater frequency separation of the rovibrational transition in the IR than the associated rotational transitions in the THz. For these same reasons, all other transitions have larger $\Pi(\nu_j)$ values because their isolated DR signature $\Delta\alpha_j$ is weaker. In other words, at atmospheric pressure the

ro-vibrational transition that makes the largest contribution to $\Delta\alpha$ is $Q_6(12)$, not $Q_2(12)$ as at low pressure (Figure 4a).

At atmospheric pressure the 9P(20) line also excites other ro-vibrational transitions besides the $Q_K(12)$ series, namely $Q_{13}(13)$ and $P_0(1)$ (Figure 5a). These are quite weak because of the low thermal population in the respective (J_p, K_p, V_0) states. Laser lines adjacent to 9P(20) also produce new coincidences, but the DR signatures are weaker (Figure 5a). This suggests a trend that will become more obvious when CH_3Cl is studied: the overlap of ro-vibrational transitions and CO_2 laser lines can be likened to a Moire pattern formed by two overlapping grids with slightly varying spatial frequencies. Overlaps more often come in clusters of CO_2 laser lines instead of through random, isolated lines.

P- and R-type ro-vibrational transitions also manifest four THz DR components, but these occur as a triplet composed of a central doublet flanked by singlets of the opposite sign (Figure 3). The differing shapes of the P, Q, and R-dependent DR spectra, particularly the associated $\Delta\alpha_j$ sign differences, represent an additional degree of recognition specificity at a specific THz probe frequency. A typical example of a R-branch DR signature comes from the $R_3(4)$ transition in $^{13}CH_3F$, optically pumped by the 9P(32) line of a CO_2 laser (Figure 5b). A P-branch DR signature would be identical except flipped in sign. The central doublet consists of two components of the same sign separated by $\nu \sim 2(B_3 - B_0)(J + 1) = 3.4$ GHz, while the singlets of opposite sign are separated from the doublets by $\nu \sim 2B \approx 50$ GHz. Consequently, the DR signature is spread twice as far in frequency as Q-branch DR signatures. The central doublet is barely resolved and very strong at atmospheric pressure.

It is striking how sparse the THz DR spectra are in Figures 5a and b. Although $^{12}CH_3F$ and $^{13}CH_3F$ have 13 and 22 pressure-broadened coincidences, respectively, most of them occur in

clusters of adjacent ro-vibrational transitions of constant J but varying K excited by the same laser line. Consequently, there are only 5 and 2 distinguishable coincidences for $^{12}\text{CH}_3\text{F}$ and $^{13}\text{CH}_3\text{F}$, respectively, each of which has up to four frequency-resolvable THz DR components. No CO_2 laser line that excites one isotopomer excites the other. There are no DR signatures of one isotopomer within the same $2\Delta\nu_P \approx 5$ GHz window of any DR signature from the other isotopomer. Indeed, the recognition specificity matrices of $^{12}\text{CH}_3\text{F}$ and $^{13}\text{CH}_3\text{F}$ are so sparse that the isotopomers are easily distinguished through the selection of CO_2 laser line and corresponding THz probe frequency.

B. Generalizations to Other Molecules

To explore how general a result this is for stretching mode DR spectra, consider more massive or complex prolate molecules and their correspondingly smaller rotational constants. Because individual absorption strengths α_{THz} will weaken with increasing molecular mass and rotational partition function, the correspondingly reduced n_L and α_{IR} might also be expected to weaken the DR signals $\Delta\alpha_j \Pi(\nu_j)/\varepsilon$. However, the number of ro-vibrational IR coincidences and rotational state overlaps ($\Pi(\nu_j)$) increase with increasing molecular mass and complexity because the rotational spacings shrink and the peak THz absorption redshifts. These effects partially or completely compensate for the increased partition function and reduced n_L . The increasing number of coincidences with CO_2 laser lines will also add more elements to the recognition specificity matrix, permitting selection of favorable DR features in atmospheric transmission windows. Nevertheless, the specificity matrix is very large, containing approximately $60 \times 200 \times 2 = 24,000$ unique combinations of sixty CO_2 laser frequencies, two hundred 5 GHz-wide

windows from 0-1 THz, and +/- sign of $\Delta\alpha_j$, respectively. Only in the rarest of cases when two molecules excited by the same laser line and produce a DR signal of the same sign in the same 5 GHz-wide window will this affect the distinguishability of molecules through their DR signatures. Such false positive detections can be avoided by simply photo-exciting a different coincidence.

The challenge of multiple coincidences requires a strategy for identifying the strongest DR signature. Several insights from the analysis of CH₃F arise. All isotopomers (and their isotopic abundance) must be considered when identifying the strongest DR signature for a given molecule. In the case of methyl fluoride, the largest $\Delta\alpha_j\Pi(\nu_j)/\varepsilon$ for the photo-excited R-branch ro-vibrational transitions of ¹³CH₃F is 7 times larger than the strongest Q-branch-excited values in ¹²CH₃F. Only ¹³C's rarity (1% isotopic abundance) prevents ¹³CH₃F from being the preferred isotopomer.

Next, consider the factor $\left\langle\left\langle U \left| \frac{d\mu}{dQ} \right| L \right\rangle\right\rangle^2$ in $\Delta\alpha_j\Pi(\nu_j)/\varepsilon$ for these ro-vibrational transitions,

which may be expressed as the product of $(d\mu/dQ)^2$ and the quantum mechanical branching ratios in Table II. Because of the latter, Q-branch transitions are only favored when $J \approx K$. However, levels with $J \approx K$ have the weakest thermal rotational population, and these same branching ratios dramatically weaken the corresponding $\Delta J = 1$ DR signatures. For a given K , the branching ratio for Q-branch transitions tends to zero as J increases, while P- and R-branch transitions tend to 1/2. Because low K transitions have closer THz spectral spacing and comparatively larger thermal populations than high K transitions, it is evident that photo-exciting low K P- or R-branch transitions will yield the largest Π_R enhancement factors.

Other factors also favor P- and R- branch transitions over Q-branch. It has already been mentioned that the strongest DR signatures will arise when transitions near the peaks of the IR spectra are excited. For increasingly massive molecules, the rotational quantum numbers J associated with these peaks will increase, and the rotational constants B and their differences ($B_i - B_0$) will decrease. Now, consider again the $2(B_3 - B_0)(J + 1)$ spacings of the doublets in the respective transitions (ignoring higher order distortion terms) as illustrated in Figure 3. In general, features are resolvable when $2(B_3 - B_0)(J + 1) > \Delta\nu_p$. In P- and R-branch transitions, the doublet components have the same sign of $\Delta\alpha$, so decreasing $(B_3 - B_0)$ or J simply increases the overlap and effectively doubles the strength of the central doublet. By contrast, the doublet components in Q-branch transitions have opposite sign, so decreasing $(B_3 - B_0)$ or J can weaken the doublet to the point of disappearance. This explains why Q-branch transitions often have DR signatures for which $\Pi(\nu_j)$ is less than one, and, more importantly, suggests that P- and R-branch transitions are more resilient than Q-branch transitions to the tradeoff between decreasing $(B_i - B_0)$ and increasing J .

Summarizing our findings to this point, the strongest DR signatures involving vibrational stretching modes will be obtained when photo-exciting rotational transitions with low K whose J values correspond to P- or R-branch ro-vibrational transitions near the peak of the corresponding IR spectra. Although these rules were derived for symmetric top molecules, their extension to the stretching modes of other types of molecules is straightforward and simplified by the fact that many of the asymmetric rotor distortions and hyperfine splittings are unresolved within the pressure broadened linewidth of the DR signal. These transitions constitute the “overlap enhancement factor” $\Pi(\nu_j)$ for asymmetric rotors.

C. Methyl Chloride

Turning now to CH₃Cl, the calculated THz DR spectra in Figures 6 and 7 reveal that both isotopomers, CH₃³⁵Cl and CH₃³⁷Cl, exhibit many more coincidences than in CH₃F. Although it is true that the *B* rotational constant is roughly half that in CH₃F (13.3 GHz for CH₃Cl, 25.5 GHz for CH₃F), that fact alone should only double the number of DR signatures over CH₃F. Instead, CH₃³⁵Cl and CH₃³⁷Cl have 154 and 140 coincidences within one atmospheric pressure broadened linewidth, respectively, 7-10 times more than CH₃F.

The difference is caused by the fact that the laser is now coincident with the V₆ vibrational bending level rather than the V₃ stretching level. Because bending modes couple vibrational ($l = \pm 1$) and rotational (*K*) motion to produce “*l*-doubled” spectra, the selection rules and branching ratios in Table III produce much richer ro-vibrational, rotational, and THz DR spectra. (Figure 1,6,7) In particular, the $\pm K$ degeneracy is removed by large energies that are proportional to *Kl*, and ro-vibrational transitions connect states of quantum number *K* in V₀ with states of quantum number (*K-l*) in V₆. Besides doubling the number of rotational and ro-vibrational transitions, *l*-doubling introduces large energy and frequency splittings in V₆, so fewer ro-vibrational transitions occur within an atmospheric pressure broadened linewidth. Indeed, atmospheric pressure broadening never adds coincidences in CH₃Cl with adjacent, ro-vibrational transitions that preserve *J* but change *K* for a given laser line, in stark contrast with CH₃F.

Instead, it is often found that a given laser line photo-excites a complex combination of overlapping and non-overlapping P-, Q-, and/or R-branch transitions simultaneously, typically involving widely separated rotational states and THz transition frequencies (see Figures 6 and 7).

The DR signature can be understood as a collection of these individual P-, Q-, and R-branch DR signatures (Figure 3) whose strengths and frequencies vary widely based on the idiosyncracies of the constituent rotational quantum numbers, energies, and transition branching ratios. The aggregate DR spectrum for a given laser line is quite unique, providing additional specificity.

For example, consider the 9P(26) laser line which has a known low pressure coincidence with the ${}^RQ_3(6)$ ro-vibrational transition in $\text{CH}_3^{35}\text{Cl}$ (Figure 4b). At atmospheric pressure, nine more P-, Q-, and R-branch ro-vibrational transitions are photo-excited, including the entire Q-branch sequence from ${}^RQ_3(4)$ to ${}^RQ_3(8)$, plus ${}^RR_2(7)$, ${}^RP_4(8)$, ${}^RR_0(24)$, ${}^PR_0(24)$, and ${}^RP_7(31)$, producing DR spectra that span 106 – 848 GHz. Interestingly, the strongest of these features are not those associated with the known low pressure ${}^RQ_3(6)$ coincidence but with the new ${}^RR_0(24)$ coincidence. A contributing reason for this is the increased overlap of the opposite sign Q-branch doublets spaced $2(B_i - B_0)(J + 1)$ apart: $(B_6 - B_0) \approx 49$ MHz in CH_3Cl while $(B_3 - B_0) \approx 339$ MHz in CH_3F . Although the coincidences in CH_3Cl typically involve states with larger J than CH_3F , atmospheric pressure broadening causes the Q-branch doublets to overlap strongly enough to reduce $I(\nu_j)$ below 1 in most cases.

Comparing the relative strengths of the constituent transitions excited by the 9P(26) line provides helpful insights into the subtle interplay of factors that contribute to the complex DR signature. First of all, because the laser frequency is within one pressure-broadened linewidth of all ten coincident IR transitions, the strength of the corresponding DR signatures depends primarily on the branching ratio of the transition. Table III indicates that as $K \rightarrow J$, the IR transitions RR and PP grow much stronger than the PR and RP transitions. For example, the branching ratios of the IR transitions ${}^RR_2(7)$ and ${}^RP_4(8)$ are 0.229 and 0.022, respectively, explaining why their contributions to the DR signature differ by an order of magnitude (Figure

4b). Likewise, the ${}^R Q_K(J)$ branching ratios (Table III) tend to zero as $J \rightarrow K$, so inspection of the Q-branch series ${}^R Q_3(4)$ to ${}^R Q_3(8)$ in Figure 4b reveals the V_6 contributions to the Q-branch doublets disappear as J decreases.

Figures 6 and 7 suggest the strongest DR feature for almost every coincidence derives from photoexcitation of a P- or R-branch transition. Although laser coincidences usually occur with isolated P- or R-branch transitions, sometimes a sequence of laser lines coincides with a sequence of IR transitions. A prominent example involves the series of laser lines spanning $10P(26) - 10P(38)$, where coincidences that preserve $K = 9$ for odd J span ${}^P P_9(23)$ to ${}^P P_9(35)$, one per laser line. Many shorter sequences with this same Moire like overlap pattern of preserving K but changing J were found in both isotopomers.

By contrast, Q-branch transitions cluster strongly, so multiple IR transitions may be excited by a single laser line. Unlike V_3 of CH_3F for which the P-, Q-, and R-branch IR transitions are arranged in clusters that preserve J for all K (Figure 1b), l -doubling in V_6 of CH_3Cl spreads out the Q-branch transitions into clusters that preserve K for all J (Figure 1c). Consequently, a given CO_2 laser line may excite many such J -changing, K -preserving IR transitions, explaining how the $9P(26)$ line excites ${}^R Q_3(4)$ through ${}^R Q_3(8)$. When this occurs, an additional reduction in the DR signature occurs. Recall that the spacing of the transitions and the separation of the Q-branch components of opposite sign are both $\sim 2B$. As a result, the positive component of one DR feature overlaps the negative component of the preceding DR feature (Figure 4b), and the summed Q-branch DR signature is much weaker than its constituent components. Therefore, Q-branch transitions generally produce unfavorably weak DR features for bending vibrational modes, just as they did in stretching vibrational modes, but for different reasons.

So atmospheric pressure broadening typically produces overlapping sequences of Q-branch DR features with $\Pi(\nu_j) < 1$ and isolated P- and R-branch DR features with $1 < \Pi(\nu_j) < 2$. However, inspection of Table VI indicates that $\Pi(\nu_j)$ can sometimes be much larger. For example, $\Pi(\nu_j) \approx 25$ for the two DR signatures near 212 GHz associated with the ${}^R\text{P}_4(8)$ transition. Such $\Pi(\nu_j) > 2$ cases are not caused by the summation of overlapping DR signatures excited by a single IR transition, as was the case for CH_3F . Instead, these are rare instances in which very different ro-vibrational transitions excited by the same laser line produce THz DR signatures that coincidentally overlap. In the example at 212 GHz, the weak ${}^R\text{P}_4(8)$ DR signatures overlap with DR signatures 17 and 5 times stronger produced by the ${}^R\text{R}_2(7)$ and ${}^R\text{Q}_3(8)$ transitions, respectively.

The increased mass of $\text{CH}_3^{37}\text{Cl}$ lowers the vibrational energy of V_6 , so the DR spectra of $\text{CH}_3^{37}\text{Cl}$ are similar in form but different in detail to those of $\text{CH}_3^{35}\text{Cl}$. The isotopic abundances (76% and 24% for ${}^{35}\text{Cl}$ and ${}^{37}\text{Cl}$, respectively) suggest that $\text{CH}_3^{35}\text{Cl}$ will be the preferred isotopomer for remote sensing. However, if a DR signature from $\text{CH}_3^{37}\text{Cl}$ is three times stronger than any from $\text{CH}_3^{35}\text{Cl}$, the less abundant isotope could produce the strongest DR signature. Indeed, if we constrain ourselves to look at the region of greatest practical interest below 300 GHz and account for isotopic abundances, we find that the strongest DR signature for CH_3Cl is the ${}^R\text{R}_3(10)$ transition of $\text{CH}_3^{37}\text{Cl}$ at 287 GHz excited by the 9P(16) laser line.

IV. CONCLUSIONS

Our analysis has shown the potential of IR/THz DR spectroscopy for the remote recognition of a trace gas in the atmosphere given sufficient pump intensity and gas

concentration. Discrimination comes from the two dimensions of a sparse recognition specificity matrix derived from (1) the few coincidences that occur between CO₂ pump laser lines and rovibrational transitions of the analyte and (2) the unique changes in THz absorption the pump coincidences induce. The strength of the DR signature depends sensitively on the type of rovibrational transition excited by the laser coincidence and the quantum and statistical mechanics of the involved transitions. Atmospheric pressure broadening, which smears out transitions detected with traditional THz spectroscopic techniques, actually assists the IR/THz DR technique by providing more pump coincidences and more overlapping transitions for a given coincidence. These advantages allow an optimal DR signature to be selected for a given analyte, and it was shown how to calculate this from basic molecular parameters.

Generally speaking, the DR signatures for CH₃Cl are much weaker than those for CH₃F: the transition dipole moments are smaller and the rotational partition function is larger, so the rovibrational pump absorption coefficient is weaker. Weak IR absorption, particularly for molecules whose pump coincidences involve bending modes, presents the greatest challenge to DR spectroscopy, just as it has limited the performance of many optically pumped far infrared laser gases. For heavier molecules, this problem may be alleviated as the transition dipole moments tend to increase (e.g. $d\mu/dQ_6 = 0.054D$ for CH₃Br) and increasing complex vibrational energy level structures allow some selection in which vibrational mode the laser excites (e.g. a CO₂ laser may excite the V_4 , V_7 , or $3V_8^1$ vibrational modes of CH₃CN) [32, 33].

ACKNOWLEDGEMENTS

The authors gratefully acknowledge the support and scientific discussions with Jen Holt, Ivan Medvedev, Christopher Neese, Paul Helminger, and Doug Petkie. This work was partially supported by the Army's competitive in-house innovative laboratory program, the Defense Threat Reduction Agency (contract number HDTRA1-09-1-0031), and DARPA.

REFERENCES

- [1] A. Othonos, *Appl. Phys. Rev.* **83**, 1789 (1998).
- [2] D. Rosen, A. G. Doukas, Y. Budansky, A. Katz, R. R. Alfano, *Appl. Phys. Lett.* **39** 935 (1981).
- [3] J. Shah, *Ultrafast Spectroscopy of Semiconductors and Semiconductor Nanostructures* (Springer, Berlin, 1999).
- [4] A. Hogele, C. Galland, M Winger, A. Imamoglu, *Phys. Rev. Lett.* **100**, 217401 (2008).
- [5] J. C. Petersen, J. Hald, *Opt. Express* **18**, 7955 (2010).
- [6] J. O. Henningsen, J. C. Petersen, *J. Opt Soc. B.* **5**, 1848 (1988).
- [7] P. A. George, J. Strait, J. Dawlaty, S. Shivaraman, M Chandrashekhar, F. Rana, M. G. Spencer, *Nano Lett.* **8**, 4248 (2008).
- [8] H. O. Everitt, F. C. De Lucia, *Advances in Atomic, Molecular, and Optical Physics*, edited by B. Bederson, H. Walther (Academic, San Diego 1995).
- [9] C. Callegari, I Reinhard, K. K. Lehmann, G. Scoles, K. Nauta, R. E. Miller, *J. Chem. Phys.* **113**, 4636 (2000).
- [10] U. Merker, H. K. Srivastava, A Callegari, K. K. Lehmann, G. Scoles, *Physical Chemistry Chemical Physics* **1**, 2427, (1999).
- [11] T Shimizu, T. Oka, *Phys Rev A* **2**, 1177 (1970).
- [12] T. Y. Chang, T. J. Bridges, *Opt. Commun.* **1**, 249 (1970).
- [13] *Handbook of Laser Wavelength*, edited by M. J. Weber, (CRC Press 1999).
- [14] G. Dodel, *Infrared Phys. & Tech.* **40**, 127 (1999).
- [15] W. H. Matteson, F. C. De Lucia, *IEEE J. Quantum Electron.* **QE-19**, 1284 (1983).
- [16] H.O. Everitt, D. D. Skatrud, F. C. De Lucia, *Appl. Phys. Lett.* **49**, 995 (1986).

- [17] R. I. McCormick, H. O. Everitt, F. C. De Lucia, D. D. Skatrud, *IEEE J. Quantum Electron.* **QE-23**, 2069 (1987).
- [18] R. L. Crownover, H. O. Everitt, F. C. De Lucia, D. D. Skatrud, *Appl. Phys. Lett.* **57**, 2882 (1990).
- [19] S-L. Chua, C. A. Caccamise, D. J. Phillips, J. D. Joannopoulos, M. Soljagic, H. O. Everitt, J. Bravo-Abad, *Opt. Express* **19**, 7513 (2011).
- [20] T. W. Pape, F. C. De Lucia, D. D. Skatrud, *J. Chem. Phys.* **100**, 5666 (1994).
- [21] De Lucia, F. C., Petkie, D. T., Everitt, H. O., *IEEE J. Quantum Electron.* **45**, 163 (2009).
- [22] J. O. Hirschfelder, C. F. Curtiss, R. B. Bird, *Molecular Theory of Gases and Liquids* (Wiley, 1954).
- [23] W.J. Witteman, *The CO₂ Laser*, (Springer-Verlag, New York, 1987).
- [24] C. H. Townes, S. L. Schawlow, *Microwave Spectroscopy*, (Dover, New York, 1975).
- [25] Q. Song, R. H. Schwendemen, *J. Mol. Spectrosc.* **165**, 277 (1994).
- [26] J-C. Deroche, G. Graner, *Optically Pumped Far-Infrared Lasers*, edited by K. J. Button, M. Inguscio, F. Strumia, (Plenum New York, 1984).
- [27] W. Gordy, R. L. Cook, *Microwave Molecular Spectra*, (John Wiley & Sons, New York, 1970).
- [28] P. F. Bernath, *Spectra of Atoms and Molecules*, (Oxford University Press, New York, 2005).
- [29] Blanquet, G., Walrand, J.L., Dang-Nhu, M., *J. Mol. Spectrosc.* **159**, 156 (1993).
- [30] G. Tarrago, O. N. Ulenikov, G. Poussigue, *J. Physique* **45**, 1429 (1984).
- [31] D. Papousek, Z. Papouskova, D. P. Chong, *J. Phys. Chem.* **99**, 15387(1995).
- [32] A. -M. Tolonen, M. Koivusaari, R. Paso, J. Schroderus, S. Alanko, R. Anttila, *J. Mol. Spectrosc.* **160**, 554 (1993).

- [33] H. Sarkkinen, R. Paso, R. Anttila, *Infrared Phys. & Tech.* **137**, 643 (1996).
- [34] D. Papousek, J. F. Ogilvie, S. Civis, M. Winnewisser, *Journal of Molecular Spectroscopy* **149**, 109 (1991).
- [35] D. Papousek, J. Demaison, G. Wlodarczak, P. Pracna, S. Klee, and M. Winnewisser, *J. Mol. Spectrosc.* **164**, 351 (1994).
- [36] D. Papousek, R. Tesar, P. Pracna, J. Kauppinen, S. P. Belov, M. Yu. Tretyakov, *J. Mol. Spectrosc.* **146**, 127 (1991).
- [37] M. -F. Le Moal, M. Margottin-Maclou, A. Valentin, *J. Mol. Spectrosc.* **183**, 93 (1997).
- [38] S. W. Sharpe, T. J. Johnson, R. L. Sams, P. M. Chu, G. C. Rhoderick, P. A. Johnson, *Appl. Specrosc* **58**, 1452 (2004).

TABLE CAPTIONS

TABLE I. Molecular constants of methyl fluoride.

TABLE II. Molecular constants of methyl chloride.

TABLE III. Branching ratios for transitions involving ground state/stretching and *l*-doubled bending vibrational states. [30]

TABLE IV. Optically pumped far-infrared laser coincidences for methyl fluoride and methyl chloride.

TABLE V. Atmospheric pressure DR parameters for $^{12}\text{CH}_3\text{F}$ and $^{13}\text{CH}_3\text{F}$.

TABLE VI. Abbreviated table of atmospheric pressure DR parameters for $\text{CH}_3^{35}\text{Cl}$. The complete table may be found in the attached appendix.

FIGURE CAPTIONS

FIG. 1. Infrared spectra of a) CO₂ laser [23], b) CH₃F, and c) CH₃Cl [28, 38] between 900 – 1100 cm⁻¹. Rotational THz spectra of d) J = 8 - 9 in V₃ = 1 of CH₃F and e) J = 8 - 9 in V₆ = 1 of CH₃Cl.

FIG.2. (color online) The calculated $\Pi(\nu_j)$ for each Q_K(12) transition of ¹²CH₃F pumped by the 9P(20) CO₂ laser line, overlaid by the HWHM linewidth of IR ro-vibrational transitions of CH₃F (continuous) and CH₃Cl (dashed) from 1 – 760 Torr.

FIG. 3. (color online) Energy level diagram depicting the IR transition (black dashed arrow) and THz rotational transitions (red and blue solid arrows) connecting the pumped states J_P, K_P and J' _P, K' _P (left). The two pairs of THz DR signatures induced by the IR pump are illustrated for the V_i (dotted red) and V₀ (dashed blue) vibrational levels, the sum of which for the three types of IR transition (P, Q, R-type) produces the measurable DR signature (right).

FIG. 4. a) (color online) Aggregate DR signature for the ¹²CH₃F transitions pumped by the 9P(20) laser line, plotted above the constituent labeled components from Table V (to scale). Energy level diagram depicting both infrared pump transitions and rotational transitions connected to the pumped states. b) Aggregate DR signature for the CH₃³⁵Cl transitions pumped by the 9P(26) laser line, plotted above the constituent components (to scale) labeled center.

Energy level diagram depicting both infrared pump transitions and rotational transitions connected to the pumped states. The transitions ${}^P R_0(24)$, ${}^R R_0(24)$ and ${}^R P_7(31)$ from Table VI are not depicted because they occur at higher frequencies.

FIG. 5. Calculated DR signatures for all laser coincidences with a) ${}^{12}\text{CH}_3\text{F}$ and b) ${}^{13}\text{CH}_3\text{F}$. The coincident CO_2 laser lines are listed on the right.

FIG. 6. Calculated DR signatures for all laser coincidences with $\text{CH}_3{}^{35}\text{Cl}$. The coincident CO_2 laser lines are listed on the right.

FIG. 7. Calculated DR signatures for all laser coincidences with $\text{CH}_3{}^{37}\text{Cl}$. The coincident CO_2 laser lines are listed on the right.

TABLE I*

	$^{12}\text{CH}_3\text{F}$ [34]		$^{13}\text{CH}_3\text{F}$ [35, 36]	
	$V_3=0$	$V_3=1$	$V_3=0$	$V_3=1$
A (MHz)	155352.70 (36)	155058.474 (19)	155365.345 (40)	155076.4480 (309)
B (MHz)	25536.14980 (54)	25197.51060 (87)	24862.665 (2)	24542.131 (3)
D_j (kHz)	60.2214 (20)	56.8868 (33)	57.72435 (1130)	55.06939 (1050)
D_{jk} (kHz)	439.8156 (240)	518.2386 (471)	424.83 (11)	477.773 (140)
D_k (kHz)	2108.0 (75)	2014.9000 (3358)	2137.293 (1881)	2071.5 (39)
H_j (Hz)	-0.03214 (93)	-0.19320 (29)	-0.02130 (728)	-0.1200 (66)
H_{jjk} (Hz)	1.9470 (275)	16.07690 (5156)	1.5360 (872)	9.7025 (1510)
H_{jkk} (Hz)	22.3610 (1601)	-96.44947 (48566)	21.500 (764)	-38.421 (1130)
H_k (Hz)	0	0.1197871 (22754)	150.4 (2471)	231.99 (138)
L_j (mHz)	0	0.01020 (87)	0	0
L_{jjk} (mHz)	0	-1.7468 (187)	0	-0.7732 (594)
L_{jkk} (mHz)	0	29.5648 (2138)	0	13.300 (504)
L_{jkkk} (mHz)	0	-173.2365 (14660)	0	-89.64 (270)
L_k (mHz)	0	0	0	0
Vibrational Energy (cm^{-1})	-	1048.610701 (10)	-	1027.49320 (2)
Dipole (debye) [31]	1.857	1.857	1.857	1.857
Dipole Derivative (debye) [31]	-	-0.271	-	-0.271

* Uncertainties in the least significant digit(s) are in parentheses.

TABLE II[†]

	¹² CH ₃ ³⁵ Cl [37]		¹² CH ₃ ³⁷ Cl [37]	
	V ₆ =0	V ₆ =1	V ₆ =0	V ₆ =1
A (MHz)	156051.1	156810.71 (2)	156440	157197.02 (3)
B (MHz)	13292.8752 (63)	13243.8840 (69)	13088.1660 (93)	13039.967 (10)
D _j (kHz)	18.1010 (39)	18.1360 (45)	17.5630 (78)	17.5960 (87)
D _{jk} (kHz)	198.77 (13)	203.37 (14)	193.48 (13)	197.85 (28)
D _k (kHz)	2653.1	2735.2 (1)	2501.0	2583.0 (1)
H _j (Hz)	-0.00845 (840)	-0.01010 (96)	-0.0121 (20)	-0.0140 (23)
H _{ijk} (Hz)	0.312 (33)	0.375 (36)	0.312 (33)	0
H _{ikk} (Hz)	9.53 (66)	5.16 (72)	8.39 (66)	4.08 (190)
H _k (Hz)	0	0	0	0
A _z (MHz)	0	39275.246 (30)	0	39560.346 (33)
q (MHz)	0	3.639735 (250)	0	3.58087 (33)
q _i (kHz)	0	-0.01724 (10)	0	-0.017850 (17)
q _{ii} (Hz)	0	0	0	0
η _i (MHz)	0	0.467059 (78)	0	0.457777 (60)
η _k (MHz)	0	4.02759 (100)	0	3.4039 (15)
η _{ik} (kHz)	0	0.12860 (57)	0	0.1267 (10)
η _{ii} (Hz)	0	-0.6601 (250)	0	0
η _{kk} (kHz)	0	-0.1020 (45)	0	-0.1250 (75)
Vibrational Energy (cm ⁻¹)	-	1018.07110 (7)	-	1017.69545 (1)
Dipole (Debye) [31]	1.8989	1.8989	1.8989	1.8989
Dipole Derivative (Debye) [31]	-	-0.0388	-	-0.0388

[†] Uncertainties in the least significant digit(s) are in parentheses.

TABLE III

Transition	Branching Ratio	<i>l</i> -Doubled Transition	Branching Ratio
$P_k(J)$	$\frac{J^2 - K^2}{J(2J + 1)}$	${}^R P_k(J)$	$\frac{(K - J)(K - J + 1)}{4J(2J + 1)}$
$\Delta J = -1,$ $\Delta K = 0$		${}^P P_k(J)$	$\frac{(-K - J)(-K - J + 1)}{4J(2J + 1)}$
$Q_k(J)$	$\frac{K^2}{J(J + 1)}$	${}^R Q_k(J)$	$\frac{(J - K)(J + K + 1)}{4J(J + 1)}$
$\Delta J = 0,$ $\Delta K = 0$		${}^P Q_k(J)$	$\frac{(J + K)(J - K + 1)}{4J(J + 1)}$
$R_k(J)$	$\frac{(J + 1)^2 - K^2}{(J + 1)(2J + 1)}$	${}^R R_k(J)$	$\frac{(J + K + 1)(J + K + 2)}{4(J + 1)(2J + 1)}$
$\Delta J = 1,$ $\Delta K = 0$		${}^P R_k(J)$	$\frac{(J - K + 1)(J - K + 2)}{4(J + 1)(2J + 1)}$

TABLE IV

Molecule	Laser Line	IR Transition	IR Transition Offset (MHz)	R_0^- (GHz)	R_0^+ (GHz)	R_1^- (GHz)	R_1^+ (GHz)
$^{12}\text{CH}_3\text{F}$	9P(20)	$Q_2(12)$	39.78 [25]	612.409	663.365	604.297	654.582
$^{13}\text{CH}_3\text{F}$	9P(32)	$R_3(4)$	-24.25 [25]	198.855 [36]	248.559 [36]	245.350 [36]	294.406 [36]
$^{12}\text{CH}_3^{35}\text{Cl}$	9P(26)	$^R Q_3(6)$	20 [26]	159.477	186.050	158.894	185.370
$^{12}\text{CH}_3^{35}\text{Cl}$	9R(12)	$^R R_6(11)$	-30 [26]	292.190	318.733	317.569	344.009
$^{12}\text{CH}_3^{37}\text{Cl}$	9P(38)	$^R P_3(13)$	-50 [26]	340.093	366.227	312.806	338.850

TABLE V[‡]

Laser Line	IR Transition	IR Transition Offset (GHz)	\mathbf{R}_0^-	\mathbf{R}_0^+	\mathbf{R}_i^-	\mathbf{R}_i^+
			V_j (GHz) $\Delta\alpha(v_j)/\epsilon$ ($\text{km}^{-1}\text{kJ}^{-1}$) $\Pi(v_i)$	V_j (GHz) $\Delta\alpha(v_j)/\epsilon$ ($\text{km}^{-1}\text{kJ}^{-1}$) $\Pi(v_i)$	V_j (GHz) $\Delta\alpha(v_j)/\epsilon$ ($\text{km}^{-1}\text{kJ}^{-1}$) $\Pi(v_i)$	V_j (GHz) $\Delta\alpha(v_j)/\epsilon$ ($\text{km}^{-1}\text{kJ}^{-1}$) $\Pi(v_i)$
¹²CH₃F						
9P(18)	Q ₁ (1)	-2.135 {1}	-	102.141{1}	-	100.786{1}
			-	-4.43	-	4.38
			-	0.27	-	0.25
9P(20)	Q _{1:7} (12)	0.042 {2}	612.072 {6}	663.000{6}	603.900{6}	654.152{6}
			61.03	-69.14	-60.22	68.22
			3.06	3.04	3.05	3.04
	Q ₁₃ (13)	-1.198 {13}	-	712.291 {13}	-	702.391 {13}
			-	-1.61	-	1.59
			-	1.03	-	0.80
	P ₀ (1)	1.585 {0}	51.072 {0}	102.143 {0}	-	50.395 {0}
			7.64	-10.18	-	7.54
			1.90	1.00	-	1.93
9P(22)	Q _{14:16} (18)	0.0007 {15}	914.385 {15}	965.016 {15}	901.451 {15}	951.385 {15}
			1.85	-2.41	-1.83	2.37
			1.77	1.74	1.74	1.72
¹³CH₃F						
9P(08)	R _{0:16} (20)	0.535 {10}	992.507 {3}	1041.930 {3}	1028.550 {3}	1077.320 {3}
			300.50	-315.75	-311.70	326.72
			4.49	4.62	4.60	4.46
9P(32)	R _{0:4} (4)	-0.025 {3}	198.887 {0}	248.598 {0}	245.394 {0}	294.458 {0}
			112.30	-136.47	-134.71	158.70
			2.92	4.40	4.38	3.55

[‡] The K quantum number of the transition closest to the CO₂ laser line is listed in {brackets} beside the IR transition offset frequency. The K quantum number of the transition with the lowest $\Pi(v)$ is listed in {brackets} beside the THz DR frequencies, and the values of $\Delta\alpha/\epsilon$ and $\Pi(v)$ are only listed for these transitions.

TABLE VI

Laser Line	IR Transition	IR Transition Offset (GHz)	\mathbf{R}_0^-	\mathbf{R}_0^+	\mathbf{R}_i^-	\mathbf{R}_i^+
			V_j (GHz)	V_j (GHz)	V_j (GHz)	V_j (GHz)
			$\Delta\alpha(v_j)/\epsilon$ ($\text{km}^{-1}\text{kJ}^{-1}$)	$\Delta\alpha(v_j)/\epsilon$ ($\text{km}^{-1}\text{kJ}^{-1}$)	$\Delta\alpha(v_j)/\epsilon$ ($\text{km}^{-1}\text{kJ}^{-1}$)	$\Delta\alpha(v_j)/\epsilon$ ($\text{km}^{-1}\text{kJ}^{-1}$)
			$\Pi(v_j)$	$\Pi(v_j)$	$\Pi(v_j)$	$\Pi(v_j)$
09P(26)	${}^R\text{Q}_3(4)$	1.09	106.324	132.902	-	132.416
			0.072	-0.128	-	0.072
			1.008	-0.500	-	0.763
	${}^R\text{Q}_3(5)$	0.60	132.902	159.477	132.416	158.894
			0.263	-0.364	-0.148	0.268
			0.243	-0.150	-0.371	0.136
	${}^R\text{Q}_3(6)$	0.02	159.477	186.050	158.894	185.370
			0.533	-0.669	-0.394	0.550
			0.102	-0.676	-0.092	0.724
	${}^R\text{R}_2(7)$	-1.28	186.064	212.636	211.858	238.329
			0.457	-0.528	-0.482	0.557
			0.990	1.709	1.825	0.951
	${}^R\text{Q}_3(7)$	-0.66	186.050	212.620	185.370	211.843
			0.760	-0.905	-0.624	0.787
			0.595	0.998	-0.637	-1.115
	${}^R\text{Q}_3(8)$	-1.44	212.620	239.187	211.843	238.312
			0.815	-0.942	-0.709	0.847
			-1.108	-0.244	1.238	0.630
	${}^R\text{P}_4(8)$	0.69	212.598	239.162	185.351	211.821
			0.041	-0.049	-0.024	0.033
			-22.055	-4.862	-16.765	-26.324
	${}^R\text{R}_0(24)$	1.04	637.057	663.512	661.071	687.418
			2.316	-2.410	-2.397	2.491
			0.970	1.425	1.430	0.971
	${}^P\text{R}_0(24)$	1.13	637.057	663.512	661.075	687.422
			2.244	-2.335	-2.323	2.414
			1.001	1.471	1.476	1.002
	${}^R\text{P}_7(31)$	-0.31	821.399	847.750	792.123	818.390
			0.162	-0.168	-0.153	0.159
			1.345	0.988	0.986	1.359

Figure 1

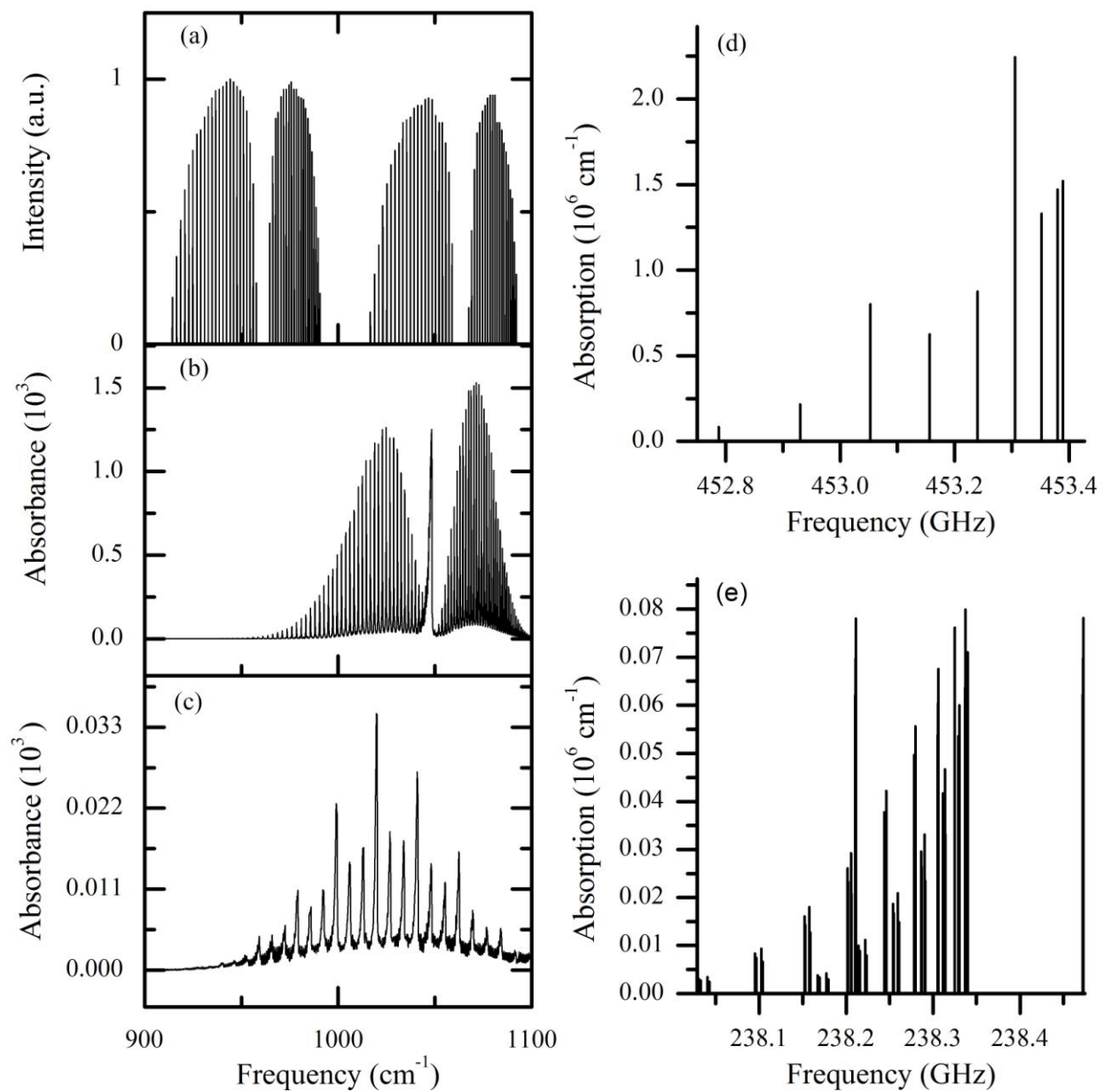


Figure 2

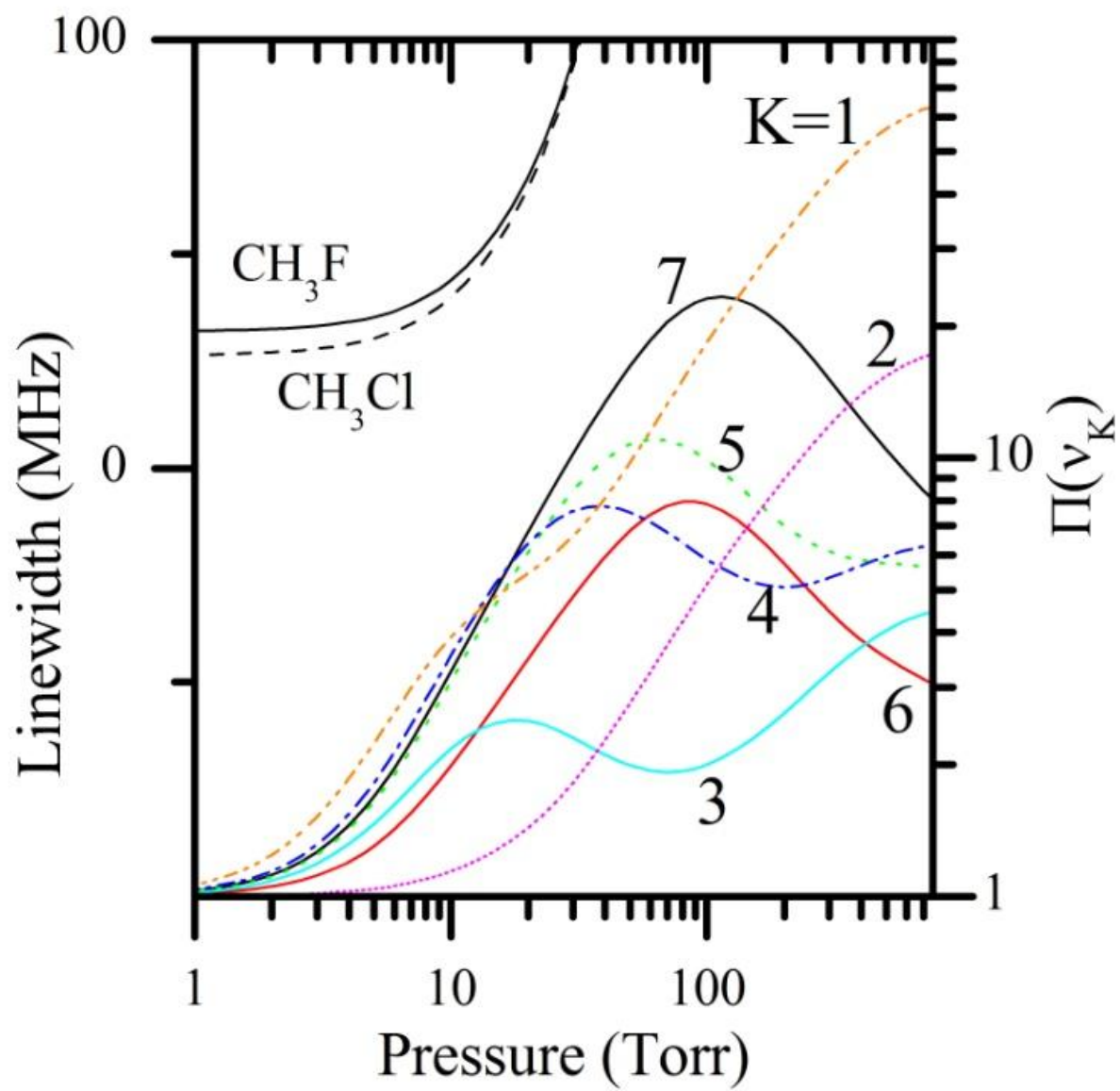


Figure 3

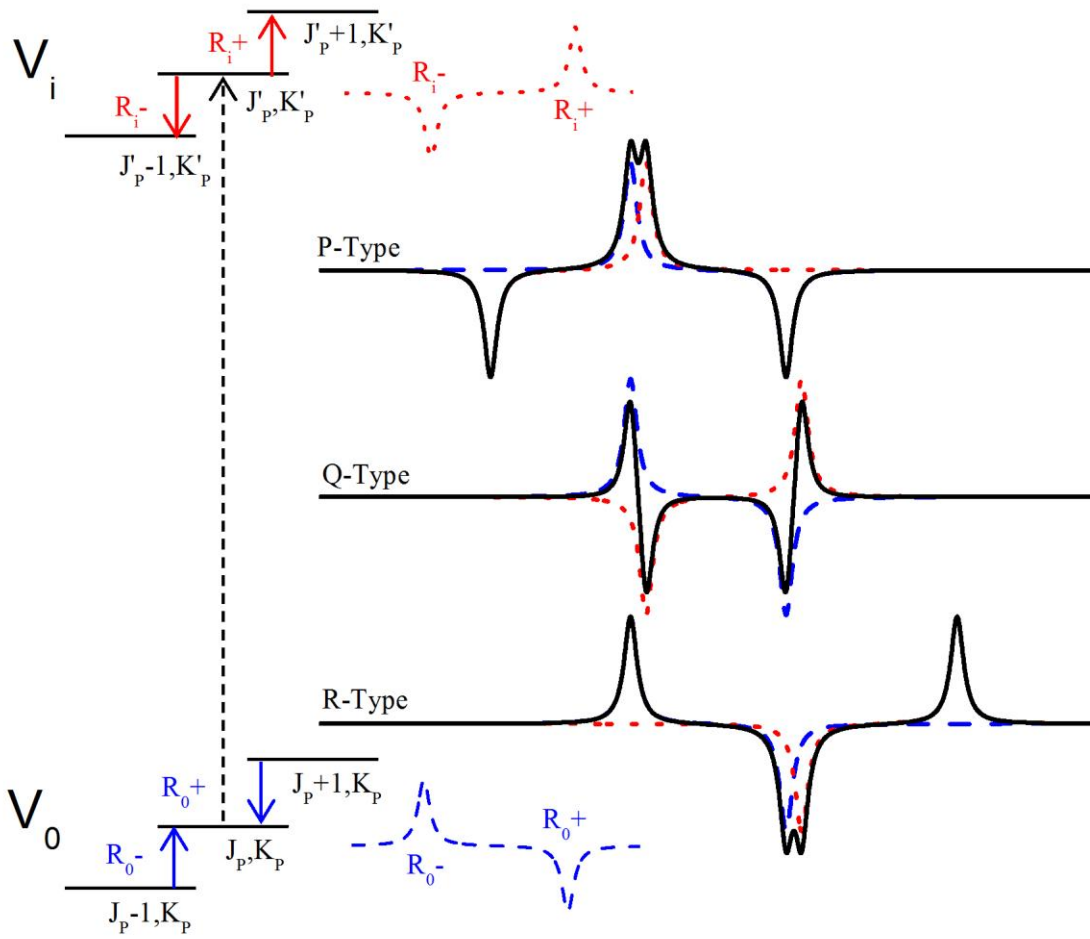
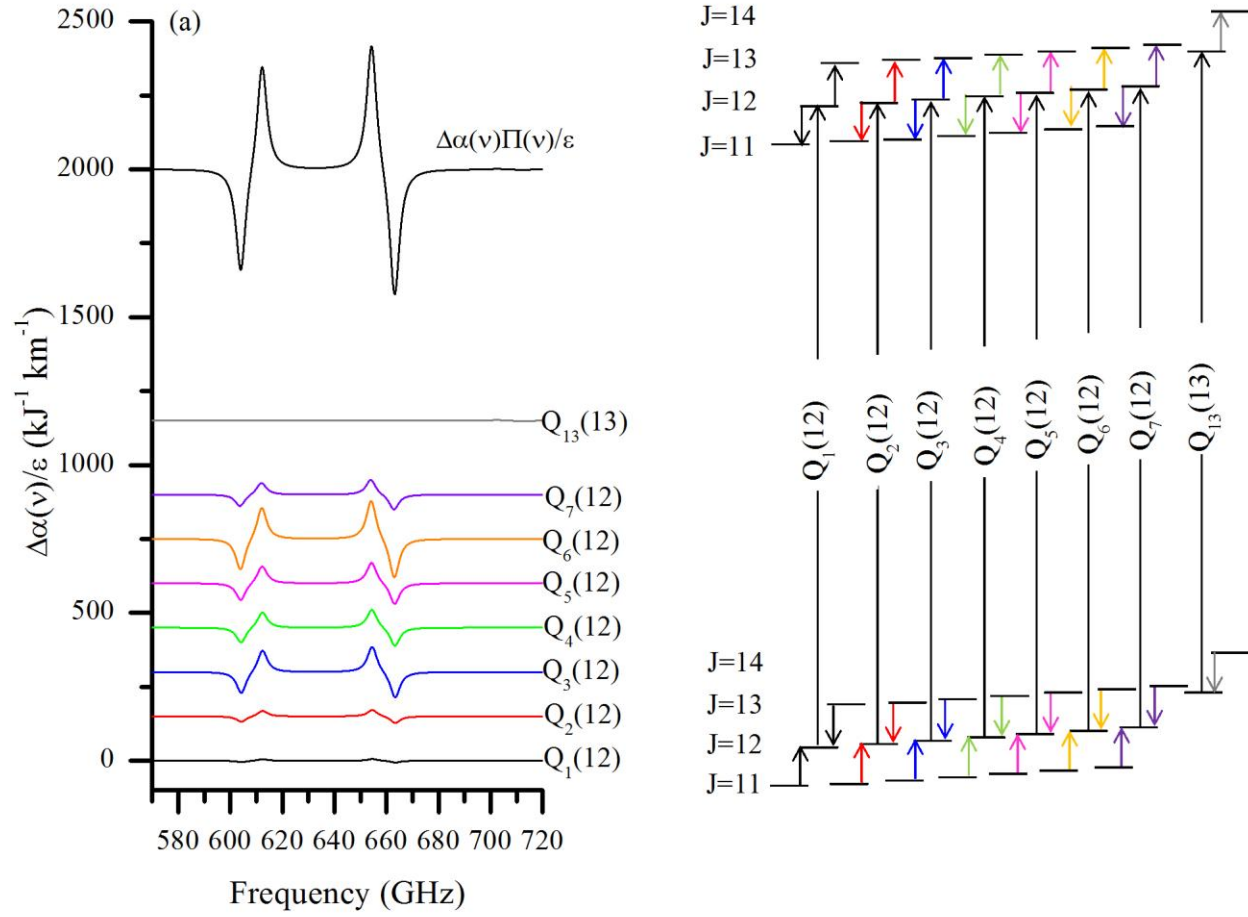


Figure 4



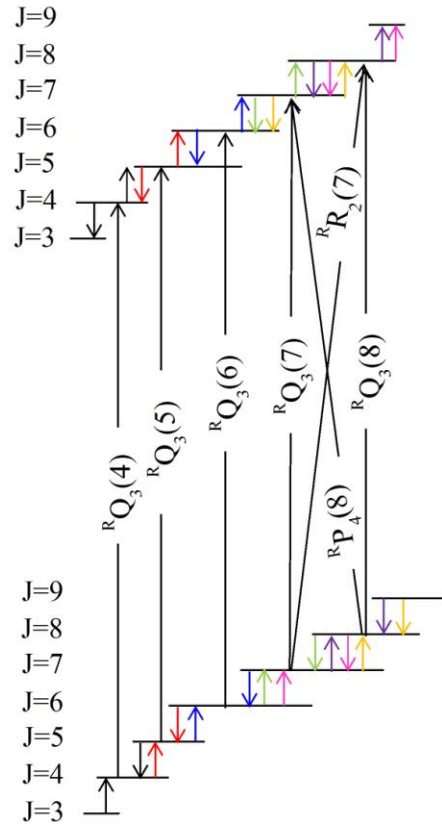
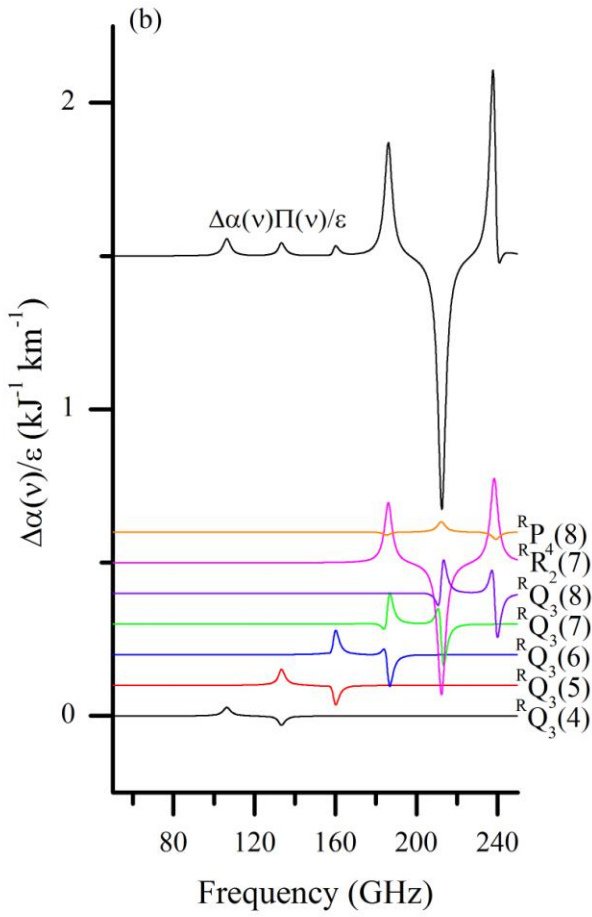


Figure 5

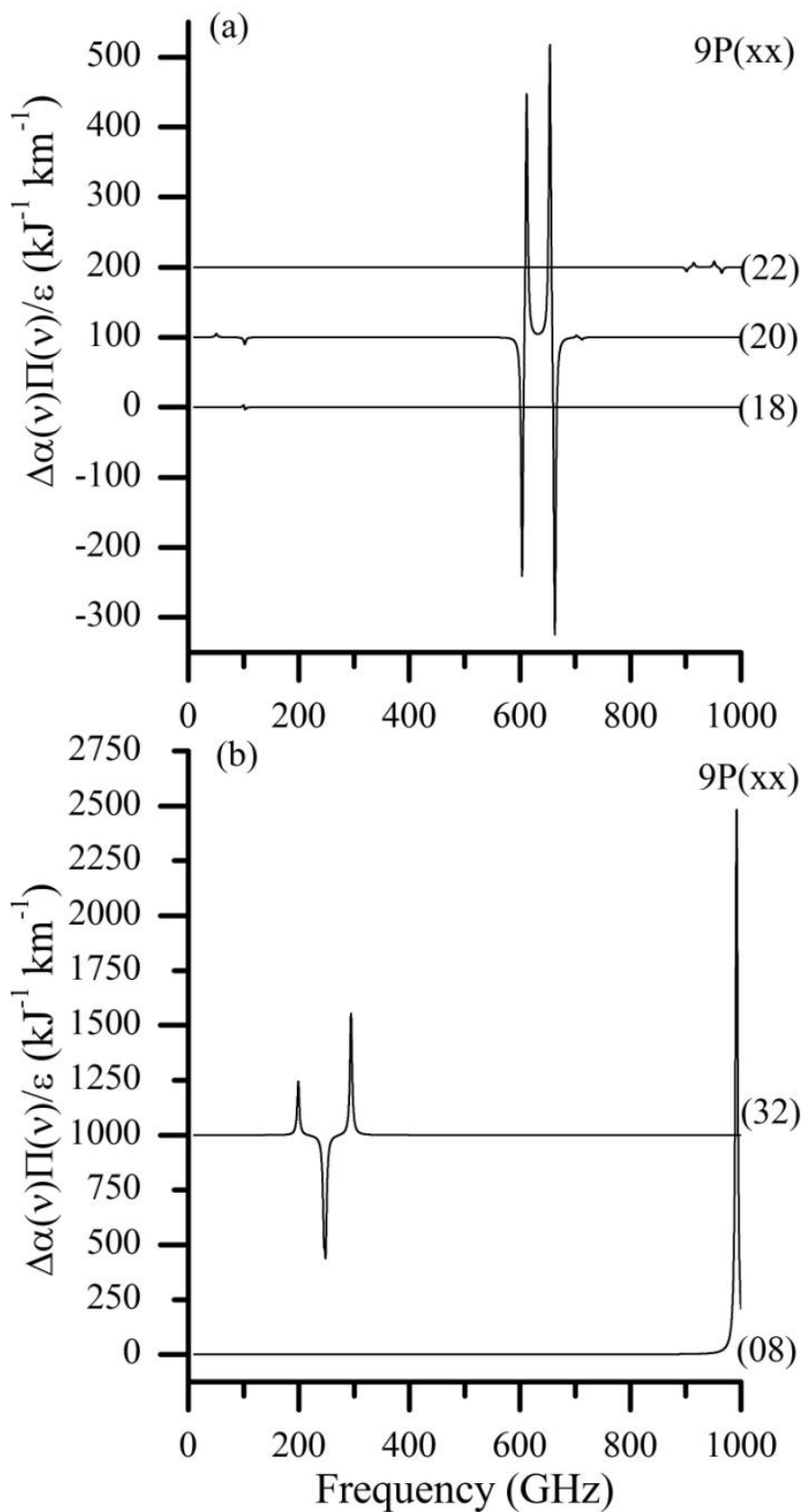


Figure 6

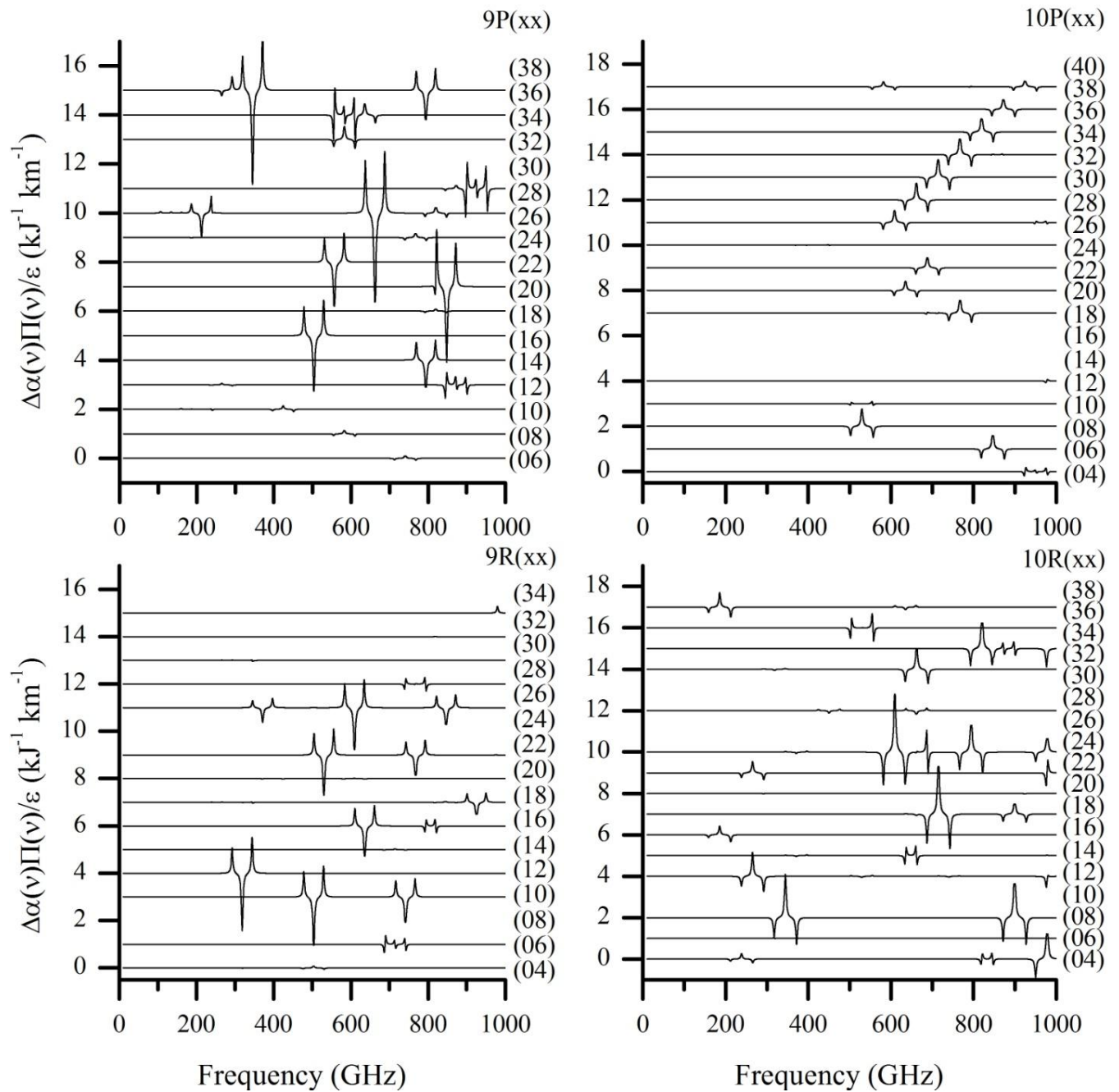
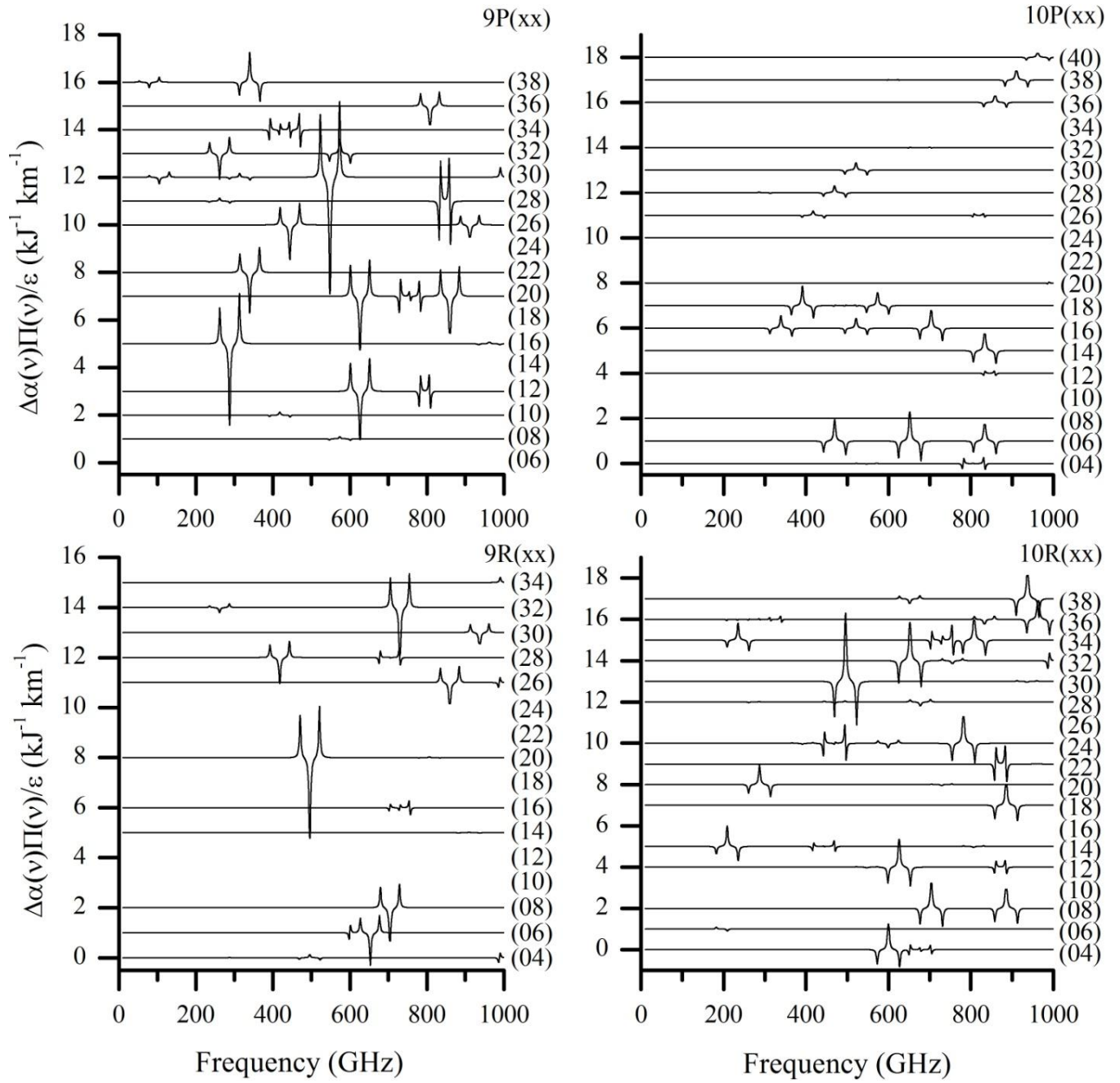


Figure 7



Appendix

CH₃³⁵Cl

Laser Line	IR Transition	IR Transition Offset (GHz)	R ₀ -	R ₀ +	R _i -	R _i +
			V _j (GHz) Δα(v _j)/ε (km ⁻¹ kJ ⁻¹) Π(v _j)	V _j (GHz) Δα(v _j)/ε (km ⁻¹ kJ ⁻¹) Π(v _j)	V _j (GHz) Δα(v _j)/ε (km ⁻¹ kJ ⁻¹) Π(v _j)	V _j (GHz) Δα(v _j)/ε (km ⁻¹ kJ ⁻¹) Π(v _j)
09P06	^R P ₉ (28)	-2.20	741.915	768.292	712.907	739.199
			0.071	-0.074	-0.066	0.069
			1.389	0.989	0.993	1.417
09P08	^R P ₈ (22)	-0.72	583.558	610.009	555.062	581.425
			0.090	-0.096	-0.081	0.087
			1.500	0.989	0.996	1.552
09P10	^R Q ₅ (6)	-0.75	159.439	186.006	0.000	185.327
			0.027	-0.050	0.000	0.027
			1.002	-0.229	0.000	0.321
	^R Q ₅ (7)	-1.43	186.006	212.570	185.327	211.793
			0.072	-0.102	-0.039	0.073
			0.158	0.003	-0.222	-0.002
	^R Q ₅ (8)	-2.20	212.570	239.130	211.793	238.256
			0.101	-0.127	-0.072	0.102
			-0.003	0.301	0.002	-0.089
	^R P ₇ (16)	-0.29	424.765	451.272	396.796	423.213
			0.085	-0.092	-0.070	0.078
			1.629	0.989	1.009	1.743
09P12	^R P ₆ (10)	-0.96	265.642	292.190	238.218	264.672
			0.038	-0.045	-0.021	0.030
			1.713	0.990	1.122	2.131
	^R Q ₅ (32)	1.03	848.053	874.399	844.944	871.192
			0.775	-0.799	-0.763	0.788
			0.638	0.197	0.714	0.395
	^R Q ₅ (33)	-2.17	874.399	900.731	871.192	897.427
			0.453	-0.467	-0.447	0.461
			-0.348	0.807	-0.697	0.611
^R P ₉ (33)	2.15	873.671	899.981	844.242	870.469	
		0.063	-0.065	-0.059	0.061	
		-1.157	4.336	9.307	5.004	
09P14	^R R ₁ (29)	1.68	769.208	795.604	792.680	818.965

			0.759	-0.785	-0.780	0.805
			0.985	1.359	1.364	0.986
	${}^R R_0(38)$	-1.64	1006.280	1032.540	1028.730	1054.880
			0.342	-0.351	-0.349	0.358
			1.014	1.282	1.284	1.014
	${}^P R_0(38)$	-1.50	1006.280	1032.540	1028.740	1054.880
			0.363	-0.372	-0.370	0.380
			0.956	1.209	1.212	0.957
09P16	${}^R R_2(18)$	1.03	478.093	504.602	502.754	529.158
			1.265	-1.335	-1.312	1.382
			0.986	1.577	1.598	0.987
09P18	${}^R P_8(31)$	-2.08	821.216	847.561	791.947	818.208
			0.058	-0.060	-0.054	0.056
			1.344	0.989	0.991	1.362
09P20	${}^R R_0(31)$	-1.07	822.000	848.370	845.244	871.503
			0.814	-0.839	-0.836	0.861
			1.477	1.836	0.924	1.003
	${}^P R_0(31)$	-0.95	822.000	848.370	845.248	871.506
			0.845	-0.872	-0.868	0.895
			1.422	1.767	0.891	0.966
	${}^R Q_4(31)$	0.67	821.803	848.167	818.789	845.056
			1.161	-1.199	-1.145	1.183
			2.040	2.584	0.161	-1.221
09P22	${}^R R_1(20)$	1.57	531.128	557.622	555.576	581.963
			1.048	-1.099	-1.087	1.139
			0.986	1.532	1.544	0.986
09P24	${}^R P_4(6)$	-1.40	159.461	186.031	0.000	158.878
			0.004	-0.006	0.000	0.002
			1.652	0.992	0.000	2.983
	${}^R P_7(29)$	1.67	768.658	795.035	739.551	765.843
			0.116	-0.121	-0.109	0.114
			1.375	0.989	0.990	1.394
09P26	${}^R Q_3(4)$	1.09	106.324	132.902	0.000	132.416
			0.072	-0.128	0.000	0.072
			1.008	-0.500	0.000	0.763
	${}^R Q_3(5)$	0.60	132.902	159.477	132.416	158.894
			0.263	-0.364	-0.148	0.268
			0.243	-0.150	-0.371	0.136
	${}^R Q_3(6)$	0.02	159.477	186.050	158.894	185.370

			0.533	-0.669	-0.394	0.550
			0.102	-0.672	-0.092	0.719
	${}^R R_2(7)$	-1.28	186.064	212.636	211.858	238.329
			0.457	-0.528	-0.482	0.557
			0.984	1.706	1.821	0.950
	${}^R Q_3(7)$	-0.66	186.050	212.620	185.370	211.843
			0.760	-0.905	-0.624	0.787
			0.592	0.996	-0.633	-1.113
	${}^R Q_3(8)$	-1.44	212.620	239.187	211.843	238.312
			0.815	-0.942	-0.709	0.847
			-1.106	-0.244	1.235	0.630
	${}^R P_4(8)$	0.69	212.598	239.162	185.351	211.821
			0.041	-0.049	-0.024	0.033
			-22.010	-4.866	-16.650	-26.263
	${}^R R_0(24)$	1.04	637.057	663.512	661.071	687.418
			1.158	-1.205	-1.198	1.245
			0.970	1.425	1.430	0.971
	${}^P R_0(24)$	1.13	637.057	663.512	661.075	687.422
			1.122	-1.167	-1.161	1.207
			1.001	1.471	1.476	1.002
	${}^R P_7(31)$	-0.31	821.399	847.750	792.123	818.390
			0.162	-0.168	-0.153	0.159
			1.345	0.988	0.989	1.361
09P28	${}^R P_7(33)$	-1.86	874.087	900.409	844.644	870.883
			0.089	-0.092	-0.085	0.088
			1.281	-9.134	0.993	1.305
	${}^R Q_3(34)$	1.45	900.946	927.270	897.637	923.863
			1.698	-1.748	-1.682	1.731
			0.631	0.193	0.696	0.197
	${}^R Q_3(35)$	-1.96	927.270	953.578	923.863	950.073
			1.255	-1.291	-1.243	1.279
			-0.268	0.706	-0.275	0.699
09P32	${}^R P_5(22)$	-0.90	583.897	610.363	555.383	581.761
			0.342	-0.359	-0.315	0.332
			1.506	0.989	0.991	1.537
09P34	${}^R Q_2(21)$	0.69	557.597	584.080	555.553	581.939
			2.201	-2.305	-2.168	2.273
			0.454	0.122	0.437	0.121
	${}^R Q_2(22)$	-1.45	584.080	610.554	581.939	608.316

			1.708	-1.785	-1.684	1.761
			-0.165	0.570	-0.163	0.325
	${}^R P_5(24)$	1.33	636.819	663.264	608.130	634.488
			0.305	-0.319	-0.284	0.298
			1.458	0.990	-2.218	1.480
09P36	${}^R P_3(11)$	-1.75	292.308	318.861	264.778	291.239
			0.330	-0.364	-0.273	0.309
			1.785	-4.271	0.996	1.897
	${}^R R_0(12)$	-0.33	318.904	345.456	344.187	370.635
			0.968	-1.045	-1.035	1.112
			0.803	1.747	1.761	0.990
	${}^P R_0(12)$	-0.28	318.904	345.456	344.190	370.639
			0.973	-1.051	-1.041	1.118
			0.798	1.737	1.752	0.984
	${}^P R_2(29)$	-0.70	769.174	795.569	792.633	818.916
			0.816	-0.844	-0.843	0.871
			0.985	1.359	1.360	0.986
	${}^P R_3(38)$	0.72	1006.150	1032.410	1028.580	1054.720
			0.652	-0.669	-0.669	0.686
			0.984	1.244	1.244	0.985
09R04	${}^R P_8(11)$	0.87	292.068	318.600	264.562	291.002
			0.004	-0.005	-0.001	0.002
			1.652	0.991	1.337	2.315
	${}^R P_9(19)$	-1.77	504.024	530.495	475.800	502.182
			0.049	-0.053	-0.042	0.046
			1.559	0.989	1.008	1.655
09R06	${}^R R_6(6)$	-0.10	0.000	185.975	185.297	211.759
			0.000	-0.328	0.000	0.327
			0.000	0.992	0.000	0.992
	${}^R Q_7(26)$	0.67	689.452	715.866	686.930	713.246
			0.635	-0.663	-0.618	0.646
			0.563	0.238	0.537	0.234
	${}^R Q_7(27)$	-1.95	715.866	742.268	713.246	739.551
			0.388	-0.404	-0.378	0.394
			-0.407	0.597	-0.399	0.576
09R10	${}^R R_3(18)$	-0.13	477.943	504.444	502.600	528.996
			1.144	-1.216	-1.172	1.245
			0.986	1.567	1.611	0.987
	${}^R R_4(27)$	1.69	716.218	742.633	739.912	766.217

			0.714	-0.741	-0.730	0.757
			0.985	1.389	1.402	0.986
09R12	$R_{R_6}(11)$	-0.03	292.190	318.733	317.569	344.009
			1.204	-1.397	-1.224	1.422
			0.986	1.681	1.889	0.987
	$R_{R_3}(38)$	-0.73	1006.150	1032.410	1028.610	1054.750
			0.883	-0.906	-0.899	0.922
			0.984	1.245	1.249	0.985
09R14	$R_{P_{11}}(27)$	1.13	715.101	741.475	686.195	712.484
			0.016	-0.017	-0.015	0.016
			1.404	0.989	0.997	1.444
09R16	$R_{R_5}(23)$	-1.47	610.363	636.819	634.488	660.836
			0.781	-0.817	-0.798	0.834
			0.985	1.461	1.484	0.986
	$R_{Q_8}(30)$	-0.10	794.858	821.216	791.947	818.208
			0.399	-0.414	-0.390	0.405
			0.631	0.642	0.609	0.629
09R18	$R_{Q_8}(9)$	1.21	238.991	265.532	0.000	264.562
			0.009	-0.017	0.000	0.009
			1.008	-0.736	0.000	0.814
	$R_{Q_8}(10)$	0.24	265.532	292.068	264.562	291.002
			0.039	-0.056	-0.020	0.039
			0.317	-0.099	-0.351	0.042
	$R_{Q_8}(11)$	-0.83	292.068	318.600	291.002	317.437
			0.069	-0.088	-0.048	0.069
			0.080	0.081	-0.034	-0.002
	$R_{Q_8}(12)$	-1.99	318.600	345.126	317.437	343.866
			0.069	-0.083	-0.054	0.070
			-0.103	0.361	0.003	0.082
	$R_{P_{12}}(32)$	-0.18	846.556	872.856	817.237	843.453
			0.021	-0.022	-0.019	0.020
			1.338	0.926	0.991	1.363
	$R_{R_4}(34)$	2.00	900.852	927.173	923.768	949.976
			0.372	-0.383	-0.379	0.390
			0.984	1.289	1.296	0.985
09R20	$R_{P_{10}}(15)$	1.09	397.949	424.443	370.092	396.495
			0.005	-0.005	-0.003	0.004
			1.617	0.990	1.085	1.911
	$R_{P_{11}}(23)$	-2.00	609.493	635.911	580.933	607.264

			0.009	-0.010	-0.008	0.008
			1.474	0.989	1.004	1.544
09R22	^R R ₆ (19)	2.20	504.361	530.850	528.910	555.293
			0.982	-1.044	-1.003	1.065
			0.986	1.541	1.587	0.986
	^R R ₅ (28)	1.68	742.533	768.933	766.116	792.405
			0.576	-0.597	-0.587	0.609
			0.985	1.372	1.386	0.986
	^R P ₁₃ (37)	0.68	977.547	1003.760	947.824	973.957
			0.004	-0.004	-0.004	0.004
			1.270	0.987	0.989	1.288
09R26	^R R ₇ (13)	-1.93	345.203	371.730	370.372	396.796
			0.322	-0.365	-0.326	0.371
			0.986	1.646	1.809	0.987
	^R P ₁₁ (19)	0.62	503.725	530.180	475.517	501.884
			0.008	-0.009	-0.006	0.007
			1.576	0.914	1.002	1.717
	^R R ₆ (22)	1.94	583.801	610.263	608.031	634.385
			1.076	-1.132	-1.098	1.154
			0.985	1.479	1.510	0.986
	^R R ₅ (31)	-1.51	821.693	848.053	844.944	871.192
			0.502	-0.519	-0.511	0.528
			0.985	1.328	1.338	0.985
09R28	^R Q ₉ (28)	1.61	741.915	768.292	739.199	765.480
			0.382	-0.398	-0.370	0.387
			0.599	-0.053	0.573	-0.044
	^R Q ₉ (29)	-1.20	768.292	794.657	765.480	791.747
			0.430	-0.448	-0.418	0.436
			0.049	0.629	0.041	0.610
09R30	^R Q ₉ (10)	0.97	265.464	291.994	0.000	290.928
			0.013	-0.024	0.000	0.013
			1.006	-0.661	0.000	0.662
	^R Q ₉ (11)	-0.10	291.994	318.519	290.928	317.356
			0.052	-0.075	-0.027	0.052
			0.307	-0.024	-0.307	0.008
	^R Q ₉ (12)	-1.26	318.519	345.039	317.356	343.779
			0.079	-0.101	-0.055	0.079
			0.023	0.401	-0.008	0.020
09R32	^R P ₁₃ (31)	0.51	819.940	846.244	790.714	816.934

			0.005	-0.005	-0.005	0.005
			1.341	0.989	0.996	1.373
09R34	${}^R R_5(37)$	-1.47	979.636	1005.910	1002.210	1028.370
			0.288	-0.296	-0.292	0.300
			0.984	1.255	1.261	0.985
10P04	${}^P Q_9(35)$	1.54	926.276	952.556	922.788	948.967
			0.260	-0.268	-0.263	0.271
			0.698	0.201	0.703	0.209
	${}^P Q_9(36)$	-2.05	952.556	978.820	948.967	975.132
			0.191	-0.197	-0.193	0.199
			-0.282	0.721	-0.294	0.725
10P06	${}^P P_5(32)$	1.46	848.053	874.399	818.641	844.902
			0.437	-0.451	-0.426	0.440
			1.332	0.989	0.988	1.328
10P08	${}^P P_7(20)$	1.44	530.747	557.222	502.385	528.770
			0.466	-0.495	-0.458	0.485
			1.578	0.988	0.983	1.531
10P10	${}^P Q_{10}(19)$	1.07	503.882	530.345	501.983	528.347
			0.121	-0.132	-0.129	0.140
			0.369	-0.019	0.447	-0.017
	${}^P Q_{10}(20)$	-0.93	530.345	556.800	528.347	554.701
			0.137	-0.149	-0.146	0.156
			0.018	0.431	0.016	0.485
10P12	${}^P R_{14}(26)$	-0.94	687.954	714.310	711.556	737.798
			0.002	-0.002	-0.002	0.003
			0.984	1.408	1.372	0.986
	${}^P R_{15}(34)$	1.05	898.070	924.309	920.714	946.835
			0.002	-0.002	-0.002	0.002
			0.982	1.285	1.269	0.933
	${}^P Q_{10}(37)$	0.39	978.544	1004.780	974.842	1000.980
			0.095	-0.098	-0.096	0.099
			0.725	0.731	0.726	0.741
10P18	${}^P Q_{11}(26)$	1.92	688.716	715.101	686.105	712.390
			0.063	-0.067	-0.066	0.069
			0.548	-0.217	0.586	-0.276
	${}^P Q_{11}(27)$	-0.79	715.101	741.475	712.390	738.663
			0.095	-0.100	-0.098	0.103
			0.152	2.721	0.193	-2.627
	${}^P P_7(29)$	-1.07	768.658	795.035	739.497	765.788

			0.393	-0.408	-0.384	0.399
			1.378	0.989	0.899	1.366
	${}^P R_{16}(35)$	-0.95	923.890	950.102	946.378	972.470
			0.000	0.000	0.000	0.000
			0.941	1.284	1.272	0.972
10P20	${}^P P_8(24)$	1.98	636.449	662.879	607.727	634.068
			0.260	-0.273	-0.256	0.268
			1.478	0.988	0.984	1.447
10P22	${}^P P_8(26)$	-1.45	689.298	715.706	660.398	686.718
			0.300	-0.314	-0.294	0.308
			1.435	0.988	0.985	1.412
10P24	${}^P Q_{12}(14)$	1.58	371.206	397.690	369.795	396.177
			0.011	-0.015	-0.015	0.020
			-0.041	-0.090	0.499	-0.363
	${}^P Q_{12}(15)$	0.06	397.690	424.167	396.177	422.553
			0.028	-0.036	-0.035	0.043
			0.050	0.043	0.202	0.100
	${}^P Q_{12}(16)$	-1.55	424.167	450.636	422.553	448.922
			0.028	-0.034	-0.033	0.039
			-0.055	0.263	-0.128	0.446
	${}^P R_{16}(28)$	2.00	740.003	766.313	763.314	789.507
			0.000	0.000	0.000	0.000
			0.984	1.366	1.333	0.986
10P26	${}^P R_{15}(18)$	-0.26	476.530	502.953	501.003	527.315
			0.000	0.000	0.000	0.000
			0.886	1.870	1.609	0.563
	${}^P P_9(23)$	2.21	609.854	636.288	581.220	607.564
			0.338	-0.358	-0.335	0.353
			1.503	0.988	0.982	1.458
	${}^P Q_{12}(36)$	0.72	951.668	977.907	948.033	974.171
			0.068	-0.070	-0.069	0.071
			0.716	0.723	0.720	0.735
10P28	${}^P P_9(25)$	1.17	662.712	689.124	633.898	660.222
			0.490	-0.514	-0.483	0.507
			1.457	0.988	0.983	1.423
10P30	${}^P P_9(27)$	0.52	715.525	741.915	686.535	712.836
			0.538	-0.562	-0.530	0.554
			1.415	0.989	0.984	1.390
	${}^P R_{18}(36)$	-2.03	949.160	975.331	971.441	997.490

			0.000	0.000	0.000	0.000
			0.927	1.281	1.268	0.960
10P32	^P P ₉ (29)	0.25	768.292	794.657	739.126	765.403
			0.497	-0.517	-0.489	0.509
			1.378	0.989	0.985	1.359
	^P Q ₁₃ (32)	0.22	846.244	872.534	842.997	869.186
			0.026	-0.027	-0.027	0.028
			0.649	0.679	0.694	0.688
10P34	^P R ₁₆ (16)	0.94	0.000	449.895	448.138	474.453
			0.000	0.000	0.000	0.000
			0.000	1.139	0.000	0.919
	^P P ₉ (31)	0.39	821.008	847.347	791.668	817.920
			0.424	-0.440	-0.417	0.432
			1.345	0.989	0.986	1.331
	^P R ₁₈ (31)	2.07	818.081	844.325	840.963	867.088
			0.000	0.000	0.000	0.000
			6355.580	1569.010	402.501	-38.064
10P36	^P P ₉ (33)	0.93	873.671	899.981	844.158	870.383
			0.317	-0.328	-0.311	0.322
			1.316	0.989	0.986	1.305
	^P R ₁₉ (36)	-0.79	948.650	974.807	970.882	996.916
			0.000	0.000	0.000	0.000
			-9.867	4.155	4.550	-0.221
10P38	^P P ₁₁ (22)	-0.34	583.065	609.493	554.519	580.856
			0.134	-0.144	-0.135	0.144
			1.535	0.988	0.976	1.456
	^P Q ₁₄ (30)	0.89	793.307	819.614	790.246	816.451
			0.013	-0.013	-0.013	0.014
			0.631	0.303	0.655	0.313
	^P Q ₁₄ (31)	-2.27	819.614	845.908	816.451	842.642
			0.007	-0.007	-0.007	0.008
			-0.569	0.682	-0.587	0.665
	^P P ₉ (35)	1.88	926.276	952.556	896.593	922.788
			0.182	-0.188	-0.179	0.184
			1.290	0.989	0.987	1.281
10R04	^P P ₇ (9)	1.87	239.044	265.591	211.703	238.154
			0.125	-0.179	-0.156	0.201
			2.286	0.989	0.884	1.466
	^P R ₁₀ (12)	-0.49	318.429	344.942	343.643	370.049

			0.002	-0.003	-0.004	0.004
			0.905	1.958	1.594	0.985
	${}^PQ_8(31)$	-0.23	821.216	847.561	818.138	844.383
			0.381	-0.395	-0.386	0.400
			0.643	0.655	0.649	0.666
	${}^PP_3(37)$	-0.50	979.870	1006.150	950.046	976.240
			0.966	-0.991	-0.940	0.965
			1.270	0.989	0.988	1.270
10R06	${}^PQ_8(9)$	0.11	238.991	265.532	238.098	264.540
			0.021	-0.041	-0.040	0.057
			-0.627	0.038	0.538	-0.081
	${}^PQ_8(10)$	-0.89	265.532	292.068	264.540	290.977
			0.049	-0.070	-0.069	0.088
			-0.032	-0.006	0.068	0.070
	${}^PQ_8(11)$	-1.98	292.068	318.600	290.977	317.410
			0.056	-0.072	-0.071	0.085
			0.008	0.070	-0.087	0.336
10R08	${}^PP_6(13)$	0.76	345.270	371.802	317.550	343.988
			1.178	-1.312	-1.173	1.298
			1.814	0.988	0.974	1.666
	${}^PP_3(34)$	0.64	900.946	927.270	871.372	897.612
			1.267	-1.304	-1.231	1.268
			1.305	0.989	0.988	1.305
10R12	${}^PP_6(10)$	-1.50	265.642	292.190	238.203	264.657
			0.617	-0.741	-0.648	0.758
			1.994	0.989	0.951	1.648
	${}^PR_{10}(19)$	-0.21	503.882	530.345	528.347	554.701
			0.027	-0.030	-0.031	0.034
			0.984	1.583	1.519	0.987
	${}^PR_{11}(27)$	1.37	715.101	741.475	738.663	764.924
			0.018	-0.019	-0.020	0.021
			0.984	1.391	1.370	0.986
	${}^PQ_7(37)$	1.69	979.286	1005.550	975.621	1001.780
			0.217	-0.223	-0.218	0.224
			0.044	-2.216	2.427	2.278
	${}^PP_2(38)$	0.85	1006.220	1032.480	976.319	1002.500
			0.424	-0.435	-0.412	0.423
			1.164	1.268	1.277	1.338
	${}^PQ_7(38)$	-2.08	1005.550	1031.790	1001.780	1027.930

			0.165	-0.170	-0.166	0.171
			2.990	3.052	-3.074	0.275
10R14	${}^P R_9(13)$	1.78	345.039	371.553	370.160	396.568
			0.016	-0.019	-0.022	0.025
			0.983	1.816	1.622	0.988
	${}^P Q_7(24)$	0.12	636.591	663.027	634.217	660.554
			0.719	-0.754	-0.734	0.768
			0.512	0.531	0.529	0.550
	${}^P R_{12}(37)$	0.71	977.907	1004.130	1000.290	1026.400
			0.017	-0.017	-0.018	0.018
			0.984	1.246	1.240	0.985
10R16	${}^P P_6(7)$	-1.64	185.975	212.535	0.000	185.285
			0.180	-0.335	0.000	0.407
			2.867	0.988	0.000	1.304
10R18	${}^P R_{10}(24)$	-1.68	636.109	662.525	660.026	686.330
			0.028	-0.029	-0.030	0.032
			0.943	1.735	1.638	-39.627
	${}^P P_3(27)$	-1.42	716.293	742.711	687.315	713.647
			1.616	-1.676	-1.561	1.621
			1.414	0.989	0.971	1.412
	${}^P P_2(34)$	-2.20	901.014	927.339	871.443	897.685
			0.376	-0.387	-0.364	0.375
			1.305	0.989	0.988	1.307
10R20	${}^P R_8(10)$	-0.11	265.532	292.068	290.977	317.410
			0.006	-0.008	-0.011	0.013
			0.979	2.007	1.633	0.989
	${}^P R_{11}(34)$	1.73	899.447	925.727	922.210	948.374
			0.013	-0.014	-0.014	0.014
			0.984	1.283	1.274	0.985
10R22	${}^P P_5(10)$	-2.23	265.686	292.238	238.245	264.703
			0.296	-0.343	-0.298	0.340
			1.939	0.989	0.967	1.708
	${}^P Q_6(37)$	-0.64	979.475	1005.740	975.821	1001.990
			0.866	-0.890	-0.869	0.893
			0.721	0.728	0.719	0.734
10R24	${}^P R_8(13)$	-0.60	345.126	371.647	370.258	396.674
			0.029	-0.034	-0.037	0.042
			0.983	1.793	1.643	0.988
	${}^P P_3(23)$	-1.46	610.509	636.971	581.881	608.255

			1.828	-1.908	-1.759	1.839
			1.494	0.560	0.988	1.489
	${}^P Q_6(24)$	1.41	636.714	663.155	634.347	660.689
			1.488	-1.556	-1.512	1.580
			-0.741	-0.036	1.051	-0.045
	${}^P Q_6(25)$	-1.05	663.155	689.586	660.689	687.021
			1.671	-1.744	-1.696	1.767
			0.034	0.553	0.042	0.564
	${}^P R_{10}(29)$	0.80	768.076	794.433	791.433	817.677
			0.040	-0.042	-0.043	0.045
			-13.605	-31.494	-21.654	-3.698
	${}^P P_2(30)$	0.15	795.569	821.951	766.336	792.633
			0.987	-1.019	-0.954	0.986
			1.319	0.979	0.962	1.303
	${}^P P_1(37)$	-0.66	979.987	1006.270	950.171	976.369
			0.501	-0.515	-0.486	0.500
			1.270	0.989	0.988	1.272
10R28	${}^P R_8(16)$	0.99	424.670	451.171	449.485	475.880
			0.056	-0.062	-0.066	0.071
			0.985	1.671	1.593	0.987
	${}^P R_0(24)$	1.74	636.288	662.712	660.222	686.535
			0.100	-0.106	-0.109	0.114
			0.985	1.452	1.428	0.986
10R32	${}^P R_7(11)$	1.32	292.133	318.671	317.484	343.918
			0.025	-0.030	-0.034	0.038
			0.983	1.875	1.681	0.988
	${}^P P_2(25)$	2.16	663.472	689.915	634.671	661.027
			0.672	-0.699	-0.646	0.672
			1.452	0.989	0.988	1.452
10R34	${}^P P_1(31)$	-0.21	821.988	848.357	792.673	818.958
			0.917	-0.946	-0.885	0.914
			1.345	0.420	0.988	1.348
	${}^P Q_5(32)$	1.00	848.053	874.399	844.902	871.150
			0.793	-0.818	-0.797	0.822
			-0.502	0.308	0.999	0.302
	${}^P Q_5(33)$	-2.25	874.399	900.731	871.150	897.383
			0.445	-0.459	-0.447	0.460
			-0.567	0.685	-0.555	0.681
	${}^R P_0(38)$	0.02	1006.280	1032.540	976.386	1002.570

			0.480	-0.492	-0.465	0.478
			1.257	0.986	0.986	1.259
	${}^P P_0(38)$	0.16	1006.280	1032.540	976.390	1002.570
			0.477	-0.490	-0.463	0.475
			1.262	0.991	0.991	1.265
10R36	${}^P Q_5(19)$	1.14	504.444	530.937	502.575	528.970
			1.057	-1.119	-1.081	1.141
			0.388	-0.032	0.415	-0.029
	${}^P Q_5(20)$	-0.83	530.937	557.422	528.970	555.356
			1.199	-1.265	-1.223	1.287
			0.030	0.441	0.027	0.461
10R38	${}^P P_4(7)$	0.34	186.031	212.598	158.872	185.344
			0.372	-0.469	-0.386	0.469
			2.115	0.989	0.952	1.695
	${}^P R_8(23)$	2.17	610.009	636.449	634.068	660.398
			0.069	-0.073	-0.074	0.078
			0.985	1.474	1.450	0.986

Laser Line	IR Transition	IR Transition Offset (GHz)	R ₀ -	R ₀ +	R _i -	R _i +
			V _j (GHz) Δα(v _j)/ε (km ⁻¹ kJ ⁻¹) Π(v _j)	V _j (GHz) Δα(v _j)/ε (km ⁻¹ kJ ⁻¹) Π(v _j)	V _j (GHz) Δα(v _j)/ε (km ⁻¹ kJ ⁻¹) Π(v _j)	V _j (GHz) Δα(v _j)/ε (km ⁻¹ kJ ⁻¹) Π(v _j)
09P08	1.96	^R P ₈ (22)	574.589	600.634	546.531	572.490
			0.056	-0.059	-0.050	0.054
			1.508	0.988	0.996	1.560
09P10	-1.65	^R P ₆ (8)	209.263	235.411	-	208.500
			0.004	-0.005	-	0.002
			1.629	0.992	-	2.999
	-0.76	^R P ₇ (16)	418.231	444.331	390.694	416.705
			0.076	-0.082	-0.063	0.070
			1.636	0.989	1.008	1.750
09P12	-1.01	^R R ₂ (23)	601.166	627.224	624.925	650.878
			1.236	-1.289	-1.273	1.327
			0.985	1.473	1.485	0.986
	-0.43	^R Q ₅ (30)	783.106	809.077	780.235	806.109
			1.028	-1.063	-1.011	1.047
			0.622	0.633	0.605	0.625
09P16	-0.57	^R R ₃ (10)	261.658	287.808	286.756	312.806
			1.695	-1.888	-1.763	1.963
			0.985	1.755	1.866	0.987
	-2.14	^R P ₉ (37)	963.820	989.670	934.506	960.274
			0.048	-0.050	-0.046	0.047
			1.274	0.988	0.990	1.286
09P20	-0.63	^R R ₁ (23)	601.192	627.252	624.951	650.904
			1.381	-1.440	-1.427	1.486
			0.985	1.474	1.483	0.986
	1.18	^R Q ₄ (28)	731.224	757.223	728.544	754.447
			1.179	-1.222	-1.161	1.204
			0.587	0.129	0.573	0.133
	-1.60	^R Q ₄ (29)	757.223	783.210	754.447	780.337
			0.954	-0.987	-0.940	0.974

			-0.165	0.618	-0.170	0.608
	-1.75	${}^R R_0(32)$	835.343	861.297	858.121	883.963
			0.582	-0.600	-0.597	0.615
			0.993	1.277	1.263	0.978
	-1.63	${}^P R_0(32)$	835.343	861.297	858.124	883.967
			0.612	-0.630	-0.627	0.646
			0.944	1.214	1.202	0.930
	0.85	${}^R P_8(33)$	860.485	886.401	831.494	857.327
			0.084	-0.087	-0.079	0.082
			-18.461	-5.621	-2.741	-15.381
09P22	-1.24	${}^R R_2(12)$	313.976	340.118	338.874	364.915
			0.862	-0.934	-0.902	0.977
			0.985	1.729	1.781	0.987
09P26	-2.01	${}^R R_1(16)$	418.527	444.646	443.017	469.033
			0.784	-0.832	-0.820	0.868
			0.985	1.637	1.655	0.986
	2.19	${}^P R_1(34)$	887.224	913.150	909.776	935.589
			0.373	-0.384	-0.383	0.393
			0.984	1.295	1.297	0.985
09P28	-1.55	${}^R P_4(10)$	261.631	287.778	234.621	260.676
			0.076	-0.086	-0.056	0.067
			1.763	0.989	1.023	1.967
	-0.67	${}^R Q_3(32)$	835.232	861.183	832.164	858.018
			2.592	-2.672	-2.564	2.645
			0.650	0.660	0.639	0.657
09P30	-1.45	${}^R R_2(3)$	78.523	104.695	104.312	130.387
			0.101	-0.172	-0.100	0.178
			0.983	1.553	2.652	0.989
	2.17	${}^R P_4(12)$	313.920	340.058	286.728	312.774
			0.103	-0.114	-0.085	0.096
			1.736	0.988	1.004	1.861
	0.14	${}^R R_0(20)$	522.965	549.053	547.036	573.018
			1.422	-1.491	-1.483	1.552
			0.982	1.537	1.544	0.983

	0.22	${}^P R_0(20)$	522.965	549.053	547.039	573.022
			1.415	-1.483	-1.475	1.543
			0.988	1.546	1.553	0.989
	-0.38	${}^P R_2(38)$	990.793	1016.660	1012.880	1038.630
			0.421	-0.432	-0.431	0.442
			0.984	1.249	1.250	0.984
09P32	-1.53	${}^R R_1(9)$	235.532	261.689	260.731	286.788
			0.527	-0.583	-0.564	0.621
			0.985	1.806	1.864	0.987
	0.13	${}^R P_5(22)$	574.919	600.979	546.844	572.818
			0.388	-0.407	-0.358	0.377
			1.513	0.988	0.990	1.545
09P34	1.64	${}^R Q_2(15)$	392.385	418.509	390.949	416.978
			1.266	-1.350	-1.233	1.319
			0.302	-0.168	0.265	-0.149
	0.11	${}^R Q_2(16)$	418.509	444.626	416.978	442.999
			2.039	-2.166	-1.991	2.120
			0.111	0.109	0.098	0.102
	-1.52	${}^R Q_2(17)$	444.626	470.737	442.999	469.014
			1.487	-1.574	-1.456	1.544
			-0.159	0.376	-0.149	0.351
09P36	-1.70	${}^P R_2(30)$	783.349	809.328	806.338	832.207
			0.543	-0.561	-0.560	0.578
			0.984	1.350	1.351	0.985
09P38	0.82	${}^R R_1(2)$	52.351	78.526	78.239	104.316
			0.087	-0.139	-0.086	0.148
			0.984	1.600	2.560	0.989
	-0.08	${}^R P_3(13)$	340.093	366.227	312.806	338.850
			0.750	-0.812	-0.650	0.715
			1.725	0.988	0.993	1.800
09R04	-1.20	${}^R P_8(11)$	287.575	313.698	260.493	286.526
			0.003	-0.004	-0.001	0.002
			1.656	0.991	1.336	2.321
	0.12	${}^R P_9(19)$	496.276	522.341	468.487	494.464

			0.077	-0.083	-0.065	0.071
			1.566	0.989	1.008	1.663
	0.92	$R_{Q_7(38)}$	990.136	1015.980	986.491	1012.240
			0.265	-0.272	-0.261	0.268
			0.726	0.731	0.713	0.728
09R06	1.19	$R_{Q_7(23)}$	600.767	626.808	598.571	624.517
			0.552	-0.580	-0.533	0.561
			0.504	-1.045	0.458	0.487
	-2.25	$R_{R_4(24)}$	627.113	653.157	650.766	676.703
			0.630	-0.658	-0.645	0.673
			0.978	1.975	1.094	0.984
	-1.10	$R_{Q_7(24)}$	626.808	652.839	624.517	650.452
			0.569	-0.597	-0.551	0.579
			1.065	2.192	-0.496	-1.038
09R08	1.32	$R_{R_4(26)}$	679.190	705.213	702.629	728.544
			0.864	-0.898	-0.883	0.917
			0.985	1.414	1.428	0.985
09R14	1.44	$R_{P_{12}(35)}$	911.233	937.090	882.105	907.879
			0.013	-0.014	-0.012	0.013
			1.295	0.988	0.992	1.315
09R16	2.27	$R_{Q_8(27)}$	704.714	730.707	702.135	728.032
			0.225	-0.235	-0.218	0.228
			0.573	-0.474	0.549	-0.447
	-0.40	$R_{Q_8(28)}$	730.707	756.687	728.032	753.916
			0.421	-0.438	-0.409	0.427
			0.264	0.606	0.249	0.587
09R20	1.77	$R_{P_{10}(15)}$	391.830	417.918	364.403	390.401
			0.003	-0.004	-0.002	0.003
			1.717	0.702	1.031	2.026
	0.28	$R_{R_6(18)}$	470.514	496.605	494.791	520.778
			1.813	-1.935	-1.851	1.975
			0.985	1.570	1.624	0.986
	-0.79	$R_{P_{12}(31)}$	807.664	833.577	778.870	804.699
			0.019	-0.020	-0.017	0.018

			1.348	0.988	0.994	1.377
09R26	0.76	${}^R R_5(32)$	835.035	860.979	857.818	883.652
			0.600	-0.619	-0.610	0.630
			0.984	1.320	1.329	0.985
	-0.50	${}^R Q_9(38)$	989.670	1015.500	986.026	1011.760
			0.270	-0.278	-0.266	0.273
			0.727	0.732	0.712	0.728
09R28	-0.86	${}^R R_7(15)$	392.124	418.231	416.705	442.710
			0.549	-0.604	-0.558	0.614
			0.985	1.623	1.731	0.986
	1.37	${}^R Q_9(26)$	678.540	704.538	676.058	701.959
			0.436	-0.456	-0.420	0.441
			0.559	0.001	0.525	0.007
	-1.21	${}^R Q_9(27)$	704.538	730.524	701.959	727.849
			0.453	-0.474	-0.439	0.460
			-0.001	0.592	-0.007	0.566
09R30	-1.67	${}^R R_5(35)$	912.826	938.728	935.276	961.065
			0.330	-0.340	-0.336	0.346
			0.984	1.282	1.289	0.984
09R32	1.41	${}^R R_8(9)$	235.314	261.446	260.493	286.526
			0.072	-0.136	-0.071	0.136
			0.981	1.435	2.596	0.989
	-1.05	${}^R R_6(27)$	705.005	731.008	728.331	754.226
			1.260	-1.310	-1.283	1.333
			0.985	1.395	1.412	0.985
09R34	-2.00	${}^R R_5(38)$	990.486	1016.340	1012.600	1038.340
			0.209	-0.215	-0.212	0.218
			0.988	1.253	1.261	0.984
	-0.73	${}^R P_{14}(38)$	988.007	1013.800	958.647	984.356
			0.002	-0.002	-0.002	0.002
			55.899	147.422	0.660	15.354
10P04	0.76	${}^P R_{12}(20)$	521.859	547.891	545.805	571.729
			0.012	-0.013	-0.014	0.015
			0.984	1.567	1.491	0.987

	1.29	${}^P R_{13}(28)$	729.583	755.524	752.621	778.449
			0.005	-0.005	-0.005	0.005
			0.967	1.516	1.450	-39.150
	1.61	${}^P Q_9(30)$	782.461	808.410	779.513	805.364
			0.354	-0.368	-0.360	0.374
			0.623	0.008	0.620	0.016
	-1.43	${}^P Q_9(31)$	808.410	834.347	805.364	831.201
			0.361	-0.375	-0.367	0.380
			-0.008	0.651	-0.016	0.661
10P06	0.79	${}^P P_7(18)$	470.424	496.510	442.677	468.672
			0.557	-0.598	-0.549	0.588
			1.656	1.005	0.980	1.585
	1.20	${}^P R_{12}(18)$	469.769	495.818	493.931	519.872
			0.007	-0.007	-0.008	0.009
			150.647	73.864	32.298	0.564
	2.02	${}^P P_6(25)$	652.964	678.990	624.597	650.535
			0.857	-0.894	-0.835	0.872
			1.462	0.988	0.986	1.445
	0.84	${}^P P_5(32)$	835.035	860.979	806.069	831.928
			0.545	-0.563	-0.531	0.548
			1.338	0.988	0.987	1.334
	0.21	${}^P R_{14}(34)$	884.690	910.542	907.007	932.741
			0.003	-0.003	-0.003	0.003
			-0.300	1.457	1.481	0.928
10P08	1.93	${}^P R_{12}(16)$	417.648	443.712	442.024	467.981
			0.002	-0.003	-0.003	0.004
			0.982	1.728	1.545	0.988
10P12	0.93	${}^P Q_{10}(32)$	834.114	860.030	830.955	856.771
			0.125	-0.129	-0.127	0.131
			0.654	0.665	0.661	0.678
10P14	2.06	${}^P P_6(32)$	834.899	860.840	805.929	831.785
			0.555	-0.574	-0.542	0.560
			1.338	0.988	0.987	1.332
10P16	1.39	${}^P P_9(13)$	339.732	365.839	312.445	338.459

			0.297	-0.359	-0.325	0.381
			1.926	0.988	0.936	1.543
	2.03	$P_{P_8(20)}$	522.472	548.535	494.544	520.518
			0.263	-0.281	-0.260	0.277
			1.589	0.988	0.980	1.528
	1.51	$P_{R_{14}(23)}$	599.475	625.460	623.046	648.920
			0.001	-0.001	-0.001	0.002
			0.721	1.810	1.702	-0.363
	0.17	$P_{P_7(27)}$	704.870	730.868	676.326	702.238
			0.531	-0.553	-0.519	0.541
			1.422	0.988	0.986	1.406
10P18	-1.52	$P_{R_{13}(13)}$	-	365.368	-	389.938
			-	0.000	-	0.000
			-	19721.500	-	13439.500
	-0.65	$P_{P_9(15)}$	391.940	418.034	364.467	390.470
			0.487	-0.554	-0.506	0.567
			1.790	0.988	0.959	1.571
	1.81	$P_{Q_{11}(18)}$	469.927	495.985	468.148	494.107
			0.041	-0.046	-0.045	0.050
			0.304	-0.229	0.447	-0.305
	-0.06	$P_{Q_{11}(19)}$	495.985	522.035	494.107	520.057
			0.077	-0.085	-0.083	0.091
			0.138	0.194	0.183	0.190
	-2.04	$P_{Q_{11}(20)}$	522.035	548.076	520.057	546.000
			0.047	-0.052	-0.051	0.055
			-0.347	4.871	-0.340	-5.539
	-1.27	$P_{P_8(22)}$	574.589	600.634	546.483	572.440
			0.357	-0.377	-0.351	0.371
			1.534	0.988	0.932	1.491
10P20	-1.14	$P_{Q_{11}(38)}$	989.090	1014.910	985.311	1011.030
			0.043	-0.045	-0.044	0.045
			0.733	0.739	0.734	0.749
10P24	1.08	$P_{R_{14}(14)}$	-	391.281	-	415.725
			-	0.000	-	0.000

			-	0.976	-	0.997
10P26	-1.93	^P P ₁₀ (16)	417.918	443.998	390.355	416.344
			0.102	-0.116	-0.107	0.120
			1.761	0.988	0.956	1.539
	1.71	^P R ₁₆ (27)	702.741	728.660	725.802	751.607
			0.000	0.000	0.000	0.000
			0.975	1.409	1.366	0.940
	-0.53	^P Q ₁₂ (31)	807.664	833.577	804.576	830.387
			0.099	-0.103	-0.101	0.105
			0.641	0.653	0.654	0.671
10P28	-0.83	^P P ₁₀ (18)	470.072	496.137	442.326	468.301
			0.176	-0.194	-0.179	0.196
			1.670	0.988	0.968	1.530
10P30	0.64	^P P ₁₀ (20)	522.195	548.245	494.268	520.227
			0.195	-0.211	-0.196	0.211
			1.599	0.988	0.974	1.505
	-1.00	^P R ₁₆ (22)	572.980	598.952	596.608	622.468
			0.000	0.000	0.000	0.000
			-6.144	2.438	2.368	0.744
10P32	1.46	^P Q ₁₃ (25)	651.692	677.667	649.192	675.066
			0.021	-0.022	-0.022	0.023
			0.523	-0.047	0.568	-0.043
	-1.14	^P Q ₁₃ (26)	677.667	703.631	675.066	700.929
			0.024	-0.025	-0.025	0.026
			0.043	0.567	0.040	0.600
10P36	-1.95	^P P ₉ (33)	860.270	886.179	831.201	857.025
			0.213	-0.220	-0.209	0.216
			1.321	0.988	0.986	1.310
10P38	0.04	^P Q ₁₄ (23)	599.475	625.460	597.162	623.046
			0.013	-0.014	-0.014	0.015
			0.472	0.496	0.541	0.559
	-0.12	^P P ₉ (35)	912.075	937.955	882.834	908.629
			0.305	-0.315	-0.300	0.309
			1.295	0.988	0.986	1.286

	-0.63	^P R ₁₉ (35)	908.370	934.145	930.358	956.010
			0.000	0.000	0.000	0.000
			13483.300	2600.890	602.381	-112.979
10P40	-1.78	^P R ₁₇ (17)	-	468.779	-	492.823
			-	0.000	-	0.000
			-	1.026	-	0.975
	2.13	^P P ₉ (37)	963.820	989.670	934.410	960.175
			0.132	-0.136	-0.130	0.134
			1.270	0.988	0.987	1.263
10R04	1.32	^P R ₁₀ (13)	339.637	365.737	364.360	390.355
			0.003	-0.004	-0.005	0.005
			0.980	1.858	1.601	0.987
	1.11	^P P ₅ (23)	600.979	627.030	572.788	598.751
			0.800	-0.838	-0.776	0.813
			1.505	0.989	0.986	1.489
	0.86	^P Q ₈ (25)	652.695	678.710	650.251	676.168
			0.419	-0.440	-0.429	0.449
			0.515	0.166	0.557	0.174
	-1.69	^P Q ₈ (26)	678.710	704.714	676.168	702.073
			0.305	-0.318	-0.311	0.324
			-0.240	0.566	-0.251	0.580
10R08	0.97	^P P ₄ (27)	705.213	731.224	676.676	702.601
			0.837	-0.869	-0.811	0.842
			1.421	0.988	0.987	1.416
	2.20	^P P ₃ (34)	887.119	913.042	857.992	883.831
			0.713	-0.734	-0.692	0.713
			1.311	0.988	0.988	1.311
10R12	-1.80	^P R ₁₀ (20)	522.195	548.245	546.178	572.119
			0.019	-0.020	-0.021	0.023
			0.975	1.591	1.532	0.825
	1.18	^P P ₄ (24)	627.113	653.157	598.836	624.793
			0.876	-0.913	-0.847	0.884
			1.482	0.988	0.987	1.473
	0.87	^P Q ₇ (33)	860.675	886.597	857.452	883.275

			0.421	-0.435	-0.425	0.438
			0.666	0.676	0.668	0.684
10R14	0.09	${}^P P_6(8)$	209.263	235.411	182.434	208.487
			0.487	-0.690	-0.591	0.761
			2.304	0.989	0.893	1.506
	0.84	${}^P Q_7(16)$	418.231	444.331	416.674	442.677
			0.454	-0.494	-0.481	0.519
			0.278	-0.006	0.356	-0.003
	-0.82	${}^P Q_7(17)$	444.331	470.424	442.677	468.672
			0.501	-0.541	-0.526	0.564
			0.006	0.344	0.003	0.397
	-0.38	${}^P R_{11}(30)$	782.002	807.936	804.863	830.684
			0.024	-0.025	-0.025	0.026
			0.984	1.345	1.330	0.985
10R18	0.00	${}^P P_2(34)$	887.185	913.109	858.062	883.903
			0.731	-0.752	-0.708	0.729
			1.311	0.988	0.988	1.312
10R20	-1.09	${}^P P_5(11)$	287.740	313.879	260.629	286.675
			0.526	-0.595	-0.521	0.584
			1.888	0.988	0.973	1.715
	1.65	${}^P R_{10}(27)$	704.341	730.320	727.560	753.428
			0.030	-0.031	-0.032	0.033
			0.984	1.398	1.379	0.985
10R22	-0.83	${}^P Q_6(33)$	860.840	886.766	857.627	883.455
			1.190	-1.228	-1.198	1.236
			0.665	0.675	0.666	0.683
	-1.96	${}^P R_{11}(37)$	963.255	989.090	985.311	1011.030
			0.010	-0.010	-0.010	0.011
			0.978	1.253	1.248	0.983
10R24	2.11	${}^P R_8(14)$	365.930	392.038	390.573	416.577
			0.022	-0.025	-0.027	0.030
			0.980	1.764	1.643	0.937
	1.10	${}^P Q_6(17)$	444.416	470.514	442.767	468.767
			1.379	-1.480	-1.434	1.531

			0.318	-0.049	0.369	-0.050
-0.64	${}^P Q_6(18)$	470.514	496.605	468.767	494.760	
		1.677	-1.790	-1.735	1.844	
		0.043	0.377	0.044	0.413	
0.93	${}^P R_9(22)$	574.446	600.484	598.228	624.159	
		0.121	-0.129	-0.133	0.140	
		0.984	1.506	1.473	0.986	
0.56	${}^P P_2(30)$	783.349	809.328	754.562	780.456	
		0.935	-0.965	-0.903	0.934	
		1.369	0.988	0.988	1.370	
10R28	0.92	${}^P R_7(9)$	235.366	261.504	260.531	286.568
		0.008	-0.011	-0.014	0.017	
		0.979	2.040	1.663	0.989	
2.23	${}^P R_8(17)$	444.233	470.320	468.563	494.544	
		0.039	-0.043	-0.045	0.048	
		0.984	1.644	1.579	0.987	
-1.55	${}^P R_9(25)$	652.532	678.540	675.989	701.888	
		0.109	-0.115	-0.118	0.123	
		0.984	1.438	1.417	0.986	
10R30	-1.18	${}^P P_3(19)$	496.803	522.895	468.967	494.971
		2.037	-2.147	-1.950	2.058	
		1.600	0.988	0.987	1.588	
-1.47	${}^P R_{10}(35)$	911.820	937.693	934.133	959.891	
		0.025	-0.025	-0.026	0.026	
		0.984	1.276	1.270	0.984	
10R32	0.35	${}^P P_2(25)$	653.273	679.311	624.913	650.865
		1.234	-1.283	-1.186	1.235	
		1.459	0.988	0.988	1.459	
-1.96	${}^P R_9(28)$	730.524	756.498	753.650	779.513	
		0.093	-0.097	-0.098	0.102	
		0.973	1.383	1.370	0.984	
0.60	${}^P Q_5(38)$	990.486	1016.340	986.788	1012.540	
		0.517	-0.531	-0.519	0.532	
		0.727	0.733	0.723	0.738	

10R34	1.21	${}^P P_4(9)$	235.480	261.631	208.553	234.611
			0.447	-0.517	-0.438	0.502
			1.957	0.988	0.973	1.755
1.96	${}^P Q_5(27)$	705.119	731.126	702.501	728.411	
		0.720	-0.748	-0.726	0.754	
		0.564	-0.262	0.573	-0.258	
-0.76	${}^P Q_5(28)$	731.126	757.122	728.411	754.310	
		1.079	-1.119	-1.088	1.128	
		0.182	0.604	0.179	0.604	
1.27	${}^P P_1(31)$	809.364	835.331	780.496	806.379	
		0.709	-0.731	-0.684	0.706	
		1.353	0.988	0.991	1.356	
10R36	1.95	${}^P Q_5(8)$	209.297	235.449	208.523	234.578
			0.136	-0.172	-0.166	0.199
			-0.101	0.008	0.270	-0.158
1.08	${}^P Q_5(9)$	235.449	261.596	234.578	260.629	
		0.282	-0.338	-0.326	0.377	
		-0.005	-0.020	0.097	-0.087	
0.11	${}^P Q_5(10)$	261.596	287.740	260.629	286.675	
		0.460	-0.532	-0.513	0.580	
		0.014	0.007	0.064	0.019	
-0.96	${}^P Q_5(11)$	287.740	313.879	286.675	312.717	
		0.492	-0.557	-0.536	0.597	
		-0.008	0.048	-0.021	0.086	
-2.12	${}^P Q_5(12)$	313.879	340.012	312.717	338.754	
		0.373	-0.416	-0.400	0.440	
		-0.072	0.189	-0.128	0.276	
-0.29	${}^P R_9(31)$	808.410	834.347	831.201	857.025	
		0.147	-0.152	-0.154	0.160	
		0.984	1.332	1.322	0.984	
1.57	${}^R P_0(37)$	964.971	990.852	935.606	961.404	
		0.368	-0.378	-0.357	0.366	
		1.242	0.962	0.962	1.244	
1.70	${}^P P_0(37)$	964.971	990.852	935.609	961.408	

			0.349	-0.358	-0.338	0.347
			1.311	1.016	1.015	1.314
10R38	0.05	${}^P R_8(24)$	626.670	652.695	650.251	676.168
			0.133	-0.140	-0.143	0.149
			0.984	1.459	1.438	0.986
	-1.41	${}^R P_0(36)$	939.075	964.971	909.792	935.606
			0.434	-0.445	-0.420	0.432
			1.319	1.013	1.012	1.321
	-1.29	${}^P P_0(36)$	939.075	964.971	909.796	935.609
			0.455	-0.467	-0.441	0.453
			1.256	0.965	0.964	1.259
